

Modeling Quantum Mechanical Scattering in Two Dimensions

A MAJOR QUALIFYING PROJECT REPORT
SUBMITTED TO THE FACULTY OF
WORCESTER POLYTECHNIC INSTITUTE
IN PARTIAL FULFILLMENT OF THE REQUIREMENTS
FOR THE DEGREE OF BACHELOR OF SCIENCE
BY

Anthony G. Gianfrancesco

Submitted: March 16, 2012

Approved:

L. Ramdas Ram-Mohan, Advisor

Marcus Sarkis, Advisor

CONTENTS

	Acknowledgments	4
I	Introduction	6
II	Scattering BCs in 1D	8
	A The action integral and a variational approach	8
	B Stealth finite elements in 1D scattering	10
	1 The source term	10
	2 The condition for no reflection at the stealth interfaces	14
	3 Parameter $\alpha(x)$ for the stealth region	16
	C Results for 1D tunneling in a double barrier resonant tunneling structure	16
III	2D scattering and stealth finite elements	21
	A Action Integral and Stealth Parameters in the Waveguide	21
	1 Source Term in a 2D waveguide	21
	B Double quantum barrier in a waveguide	22
	C Modal decomposition of wavefunction	27
	D Scattering from a bilateral symmetric potential in a waveguide	29
	E Arbitrary shapes for scattering potentials: circle and square	31
	F Arbitrary scattering potential: lens	38
	G Arbitrary scattering center: circular diffraction grating	42
	H Curved waveguides	52
	1 Boundary conditions	52
	2 Results	52
	I Additional Results	56
IV	Concluding remarks	69
	References	70

ACKNOWLEDGMENTS

This work was supported by the National Science Foundation under grant number and by DARPA. The computational resources at the Center for Computational NanoScience, WPI, and the use of finite element and sparse matrix analysis software from Quantum Semiconductor Algorithms, Inc., are gratefully acknowledged. I would also like to thank Paul Kassebaum for providing a beautiful insight into the symmetry of the waveguide problem. His group theory analysis is a great addition to this discussion. I would like to thank Andrei Ilyashenko for his work in developing the finite element codes and helping me to produce the results for this report. I would also like to thank Professor L. R. Ram-Mohan and Professor Marcus Sarkis for their helpful advice and guidance.

Abstract

The boundary conditions (BCs) in quantum mechanical scattering are examined in the context of scattering in finite, nanoscale systems, together with the corresponding need for and the implementation of derivative BCs within a finite domain. We have shown earlier that scattering boundary conditions can be consistently used with the principle of stationary action to solve for the scattered wave everywhere in one-dimensional (1D) and two-dimensional (2D) problems, and that mixed (Cauchy) BCs are essential in a variational (action integral) approach. These boundary conditions are non-trivial to implement for finite domains, and more so in open domains. We introduce the idea of totally absorbing regions, or “stealth regions,” whose material properties are adjusted to convert the Cauchy BCs into the simpler Dirichlet BCs. The action integral for scattering is directly discretized within the framework of the finite element method (FEM) to obtain numerical results using stealth finite elements. This approach provides excellent results for both open domains, as well as those with confined geometries. In 1D, we provide concrete examples and demonstrate the high accuracy achieved by this method. In the 2D examples, confined waveguide geometries, we show the efficacy of the method to obtain results that go beyond the traditional perturbative or approximate calculations by obtaining the waveguide transmission coefficients; the explicit form of the scattered wavefunction for complex scattering shapes are given. We compare these with the traditional partial wave analysis where such results are known. The methodology presented here is applied to multiple scattering from randomly placed scattering centers as a precursor to studying localization phenomena.

I. INTRODUCTION

Important features of quantum mechanics arising from the wave nature of particles are manifested in the phenomena of barrier penetration and scattering.¹⁻⁵ The tunneling of carriers through semiconductor resonant tunneling heterostructures, quantum cascade laser structures, scanning tunneling microscopes, and tunneling resistance devices provide practical applications of the effect. These are just a few recent examples in a long series of developments based on quantum mechanical scattering.

The theoretical calculation of scattering amplitudes and cross-sections in quantum mechanical scattering employs prepared states for incoming waves and implements scattering boundary conditions (BCs) for the outgoing probability current in open systems.⁶⁻⁹ In the open domain, the scattered wave is represented in terms of out-going Hankel functions. The fact that Hankel functions $H_n^{(1)}(kr)$ of all orders n have the same asymptotic behavior allows a substantial simplification in the application of the probability current boundary conditions. This traditional procedure of applying asymptotic boundary conditions, however, requires a re-examination in the context of scattering in finite nanoscale and meso-scale systems, and the corresponding implementation of derivative boundary conditions within a finite domain.

We have shown that scattering boundary conditions can be consistently used with the principle of stationary action to solve for the scattered wave everywhere in one-dimensional (1D) and two-dimensional (2D) problems, and that mixed (Cauchy) BCs are essential in a variational approach.¹⁰ We discuss this briefly in the following for the case of 1D scattering to illustrate the variational scheme. This is followed by its application to 2D calculations.

In general, the mixed BCs are difficult to implement for scattering in open domains, and for that matter in confining geometries in 2D and 3D systems. Here we show that the use of absorbing material around the scattering region (or the active region) provides a unique way of reducing the Cauchy BCs to the much simpler Dirichlet BCs. We first show that the procedure is remarkably effective in 1D, then extend it to 2D electron waveguides, and follow this with calculations for scattering from potentials in open domains. We employ the finite element method (FEM), which may be thought of as the discretization of the action integral in our numerical work. Within the variational-FEM approach, the absorbing finite elements, which have been called “stealth elements,” have their material properties modified so as to provide damping of the scattered waves that impinge on them. Their properties are

altered in a smooth manner as we go into the stealth region such that we have no reflected waves from the stealth regions.¹⁰ This naturally leads to the substantially simpler Dirichlet BCs, $\psi(\mathbf{r}) = 0$, on the periphery without affecting the solution in the interior.

The concept of stealth elements draws on the idea of “perfectly matched layers” used in the modeling of electromagnetic scattering, and was adapted to the quantum mechanical scattering in 2002¹⁰. We show that the accuracy of the calculations is substantially enhanced by the use of \mathcal{C}_1 -continuous interpolation polynomials in each finite element in 1D and 2D/

In Sec. II, we show how the action integral for scattering in 1D can be set up with Cauchy BCs, and how the problem can be transformed to one with Dirichlet BCs. This is followed by the theory of stealth finite elements, and the example of a double barrier resonant tunneling is considered. In Sec. III, we show that the electron waveguide analysis can be reduced to Dirichlet BCs with the use of stealth elements at the input and output ports. Results on scattering from an arbitrarily shaped scattering center in a 2D waveguide, such as a circle and square, are presented in Sec. III G, and the concluding remarks are given in Sec. IV.

II. SCATTERING BCS IN 1D

A. The action integral and a variational approach

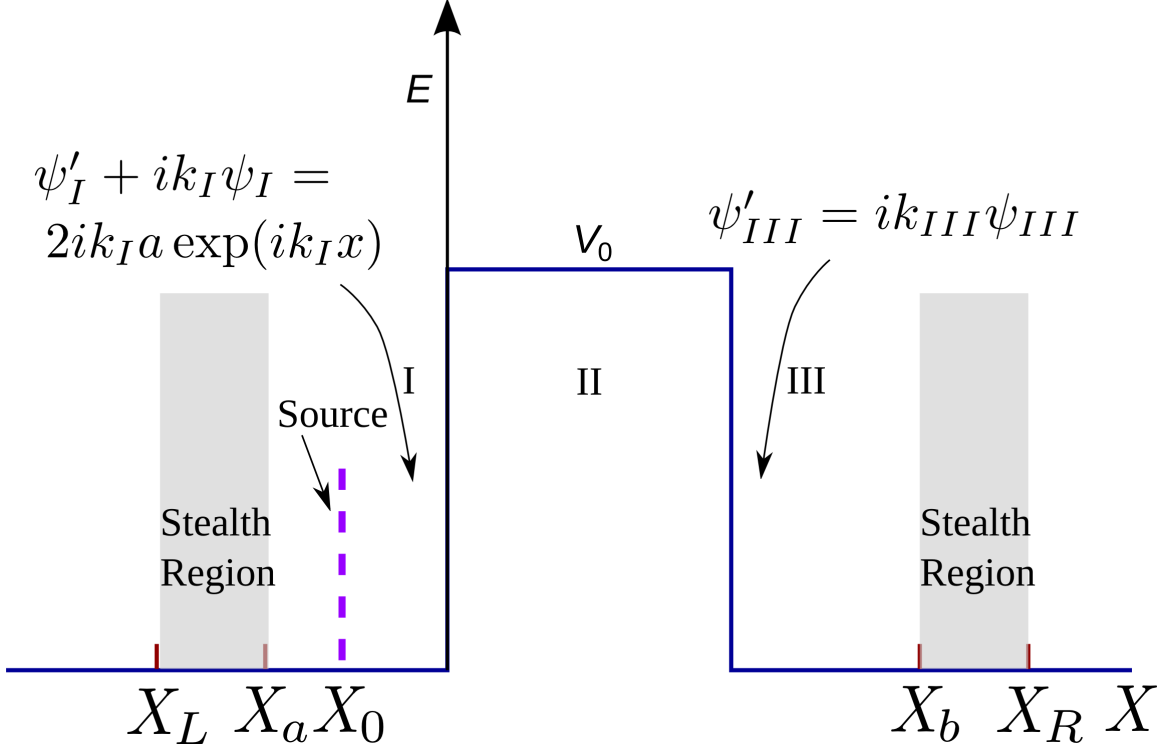


FIG. 1. A plane wave of wavevector $k_I = \sqrt{2mE/\hbar^2}$ is incident from the left on a rectangular barrier of height V_0 . The boundary conditions in regions I and III are displayed. Here $k_I = k_{III}$ for the flat potential profile.

We first show that the scattering problem can be cast in a variational form. One dimensional scattering from a barrier is particularly simple since the incident wave, $\psi_I(x) = a \exp(ikx)$, launched at $x = -\infty$ in region I in Fig. 1, and the states representing the scattered waves, $\psi_R(x) = r \exp(-ikx)$ in region I and $\psi_T(x) = t \exp(ikx)$ in region III, are readily identified. These may be viewed as a single mode of a wave incident from the left being scattered into a single reflected mode and a transmitted mode. While most textbooks treat this directly by using matching boundary conditions at the scattering potential, we employ the principle of stationary action to evaluate the reflection and transmission coefficients. The Schrödinger action is given by

$$A_0 = \int_0^T dt \int_{x_a}^{x_b} dx \left[\frac{\partial \psi^*(x)}{\partial x} \left(\frac{\hbar^2}{2m} \right) \frac{\partial \psi(x)}{\partial x} \right] + \psi^*(x) [V(x) - E] \psi(x) \quad (1)$$

We will express this in a more compact form with a new notation,

$$A_0 = \int_0^T dt \int_{x_a}^{x_b} dx \psi^*(x) \left[\overleftarrow{\partial} \left(\frac{\hbar^2}{2m} \right) \overrightarrow{\partial} + V(x) - E \right] \psi(x). \quad (2)$$

Here, the partial derivatives $\overleftarrow{\partial}$ and $\overrightarrow{\partial}$ act on functions to the left and to the right of them, respectively.

In the steady state, with a stream of particles incident on the barrier, the integration over time is performed trivially. The boundary conditions for the scattering are determined as follows. The total wavefunction at x_a in region I and its derivative

$$\begin{aligned} \psi_I(x_a) &= a \exp(ik_I x_a) + r \exp(-ik_I x_a), \\ \psi'_I(x_a) &= ik_I [a \exp(ik_I x_a) - r \exp(-ik_I x_a)], \end{aligned} \quad (3)$$

can be used to eliminate the reflected wave so that

$$\psi'_I(x_a) + ik_I \psi_I(x_a) = 2ia \exp(ik_I x_a). \quad (4)$$

Similarly, the boundary condition at x_b in region III is given by

$$\psi'_{III}(x_b) - ik_{III} \psi_{III}(x_b) = 0. \quad (5)$$

Here k_I and k_{III} are the wavevectors in regions I and III, respectively. These mixed boundary conditions of the Cauchy type can be used in the variational treatment of the scattering. The above derivative boundary conditions, Eqs. (4) and (5), require that the original action be modified by “surface terms.” A variation of A_0 with respect to $\psi^*(x)$ followed by the usual integration by parts leads to

$$\begin{aligned} \delta_{\psi^*}(A_0/T) &= \int_{x_a}^{x_b} dx \delta\psi^* \left[-\frac{\hbar^2}{2m} \frac{d^2}{dx^2} \psi(x) (V(x) - E) \psi(x) \right] \\ &+ \left(\frac{\hbar^2}{2m} \right) \left[\delta\psi^*(x_b) \frac{d\psi(x)}{dx} \Big|_{x_b} - \delta\psi^*(x_a) \frac{d\psi(x)}{dx} \Big|_{x_a} \right]. \end{aligned} \quad (6)$$

Here, neither $\psi(x_{a,b})$ nor $\psi'(x_{a,b})$ vanish. Since the surface terms are not zero at x_a and at x_b we cannot deduce Schrödinger’s equation from the integral in Eq. (6). To remedy this, it is usual¹¹ to add derivative-dependent surface terms to A_0 such that the modified action is given by

$$\begin{aligned} A/T &= \int_{x_a}^{x_b} dx \psi^*(x) \left[\overleftarrow{\partial} \left(\frac{\hbar^2}{2m} \right) \overrightarrow{\partial} + V(x) - E \right] \psi(x) \\ &- \left(\frac{\hbar^2}{2m} \right) \left[\psi^*(x_b) \frac{d\psi(x_b)}{dx} + \psi^*(x_a) \frac{d\psi(x_a)}{dx} \right]. \end{aligned} \quad (7)$$

Now the variation of A permits us to generate the equation of motion as the surface terms get eliminated. In the above, the derivatives $\psi'(x_b)$ and $\psi'(x_a)$ can be written in terms of $\psi(x_b)$ and $\psi(x_a)$ using Eqs.(4,5), and we see that the action depends on the incoming amplitude a that determines intensity of the scattering. In this sense, the boundary conditions are built into the action A .

Similar boundary conditions can be set up for electron propagation in 2D waveguides. The extension to 2D scattering in open domains is nontrivial and alternate methods would be welcome. In the following, we show how the use of absorbing (stealth) regions around the scattering region can resolve the problem of implementing scattering boundary conditions.

In the FEM, we discretize the action into small elements in each of which the original principle of stationary action holds. The wavefunctions in Eq. (2) are replaced by interpolation polynomials multiplied by coefficients associated with local “nodes” in each element. Thus, for example in 1D, in the i^{th} element with linear interpolation we have

$$\psi(x) = \frac{(x_{i+1} - x)}{(x_{i+1} - x_i)}\psi_i + \frac{(x - x_i)}{(x_{i+1} - x_i)}\psi_{i+1}. \quad (8)$$

With the assumed polynomial form in each element the spatial dependence of the action can be integrated out. We apply the variational method to the resulting bilinear form in the nodal coefficients in order to obtain the simultaneous equations that represent the discretized Schrödinger equation. In our calculations we use Hermite interpolation polynomials¹⁰ with \mathcal{C}_1 or derivative continuity to improve on the above example, Eq. (8), and to obtain excellent accuracy in numerical calculations.

B. Stealth finite elements in 1D scattering

1. The source term

Let us suppose that we place stealth regions on either end of the scattering region over $x_L \leq x \leq x_a$ and $x_b \leq x \leq x_R$. In 1D, we then require a source term at say $x = x_0$ inside the “active” region $x_a < x_0$, with x_0 located away from the localized potential (see Fig. 1). The wavefunction at x_L and x_R will be set to zero as it is completely absorbed in the stealth regions:

$$\psi(x_L) = 0 = \psi(x_R). \quad (9)$$

We consider the Schrödinger equation for the Green's function with a source term,

$$-S \frac{\hbar^2}{2m} \delta(x - x_0), \quad (10)$$

at x_0 such that the Green's function represents waves

$$G(x - x_0) = \begin{cases} a \exp(ik_0(x - x_0)), & \text{for } x > x_0; \\ a \exp(-ik_0(x - x_0)), & \text{for } x < x_0, \end{cases} \quad (11)$$

emanating in both directions from the source in the physical region. Here

$$k_0^2 = 2mE/\hbar^2. \quad (12)$$

We now identify the source coefficient S using the usual Fourier transform method. With

$$G(x - x_0) = \frac{1}{2\pi} \int_{-\infty}^{\infty} dk g(k) \exp(ik(x - x_0)) \quad (13)$$

inserted into the differential equation

$$-\frac{d}{dx} \left(\frac{\hbar^2}{2m} \frac{d}{dx} G(x - x_0) \right) - EG(x - x_0) = -S \frac{\hbar^2}{2m} \delta(x - x_0), \quad (14)$$

we obtain

$$g(k) = -\frac{S}{2k_0} \left[\frac{1}{k - k_0} - \frac{1}{k + k_0} \right], \quad (15)$$

leading to

$$G(x - x_0) = -\frac{S}{2k_0} \frac{1}{2\pi} \int_{-\infty}^{\infty} dk \left(\frac{e^{ik(x-x_0)}}{k - k_0 - i\delta} - \frac{e^{ik(x-x_0)}}{k + k_0 + i\delta} \right). \quad (16)$$

While Fourier transforming back, we have to build in the boundary conditions by closing the contour in the upper-half plane for the first term when $x > x_0$, and in the lower-half plane for the second term when $x < x_0$. The integration contours are shown in Fig. 2. We then have

$$G(x - x_0) = \frac{S}{2ik_0} \begin{cases} \exp(ik_0(x - x_0)), & x > x_0; \\ \exp(-ik_0(x - x_0)), & x < x_0. \end{cases} \quad (17)$$

The coefficient of the δ -function source term is then determined to be $S = (2ik_0a)$.

We are then able to construct the action using Dirichlet BCs at x_L, x_R in the form

$$\begin{aligned} \frac{A}{T} = & \int_{x_L}^{x_R} dx \psi^*(x) \left[\overleftarrow{\partial} \left(\frac{\hbar^2}{2m} \right) \overrightarrow{\partial} + V(x) - E \right] \psi(x) \\ & + \int dx \psi^*(x) \left(-2ik_0a \frac{\hbar^2}{2m} \delta(x - x_0) \right). \end{aligned} \quad (18)$$

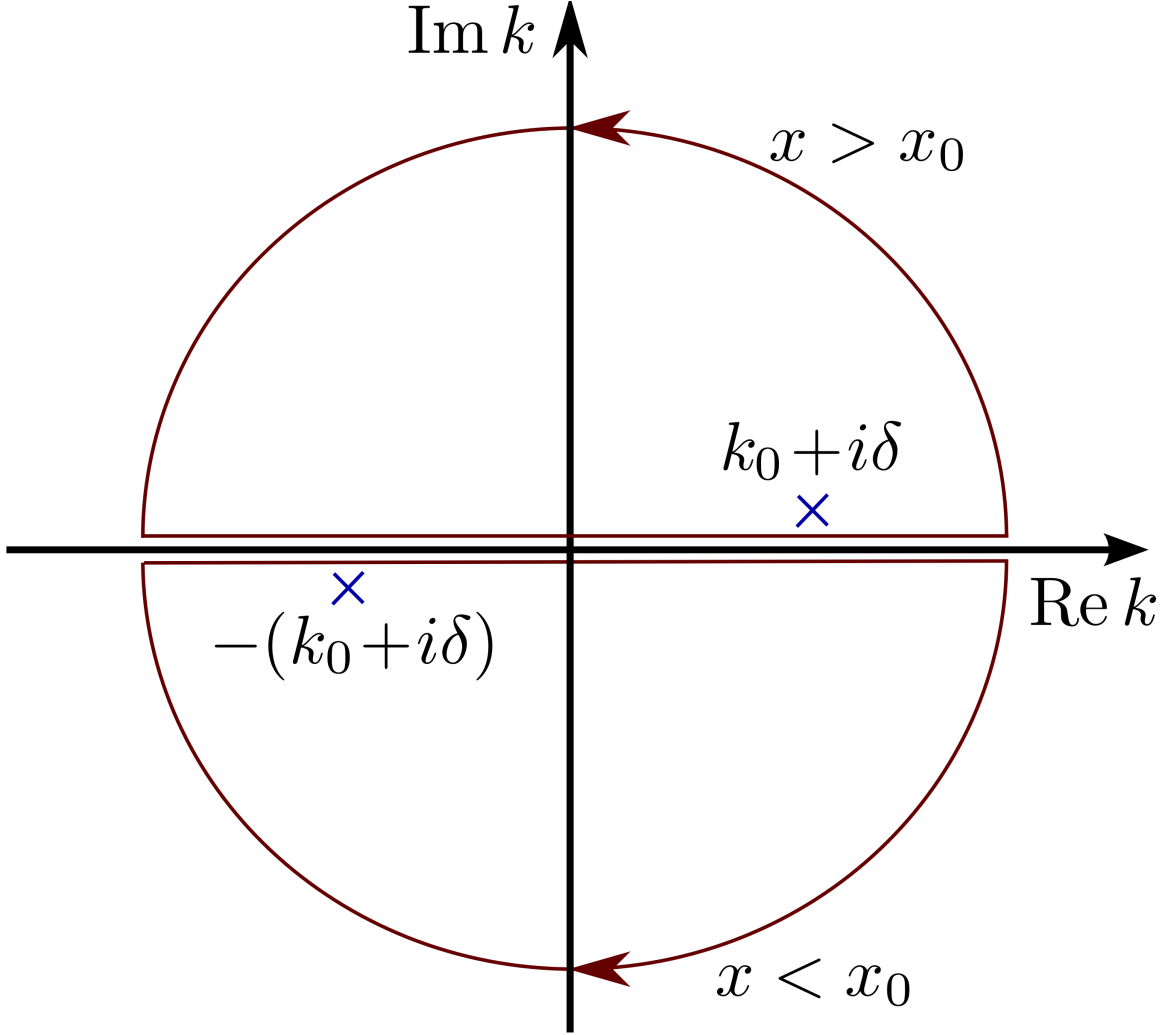


FIG. 2. The contours on the complex k -plane used to determine the Green's function are shown. For $x > 0$, we close the contour with a large semicircle in the upper-half plane enclosing the pole at $k_0 + i\delta$. For $x < 0$, the pole at $-(k + i\delta)$ is enclosed with the contour closed in the lower half plane.

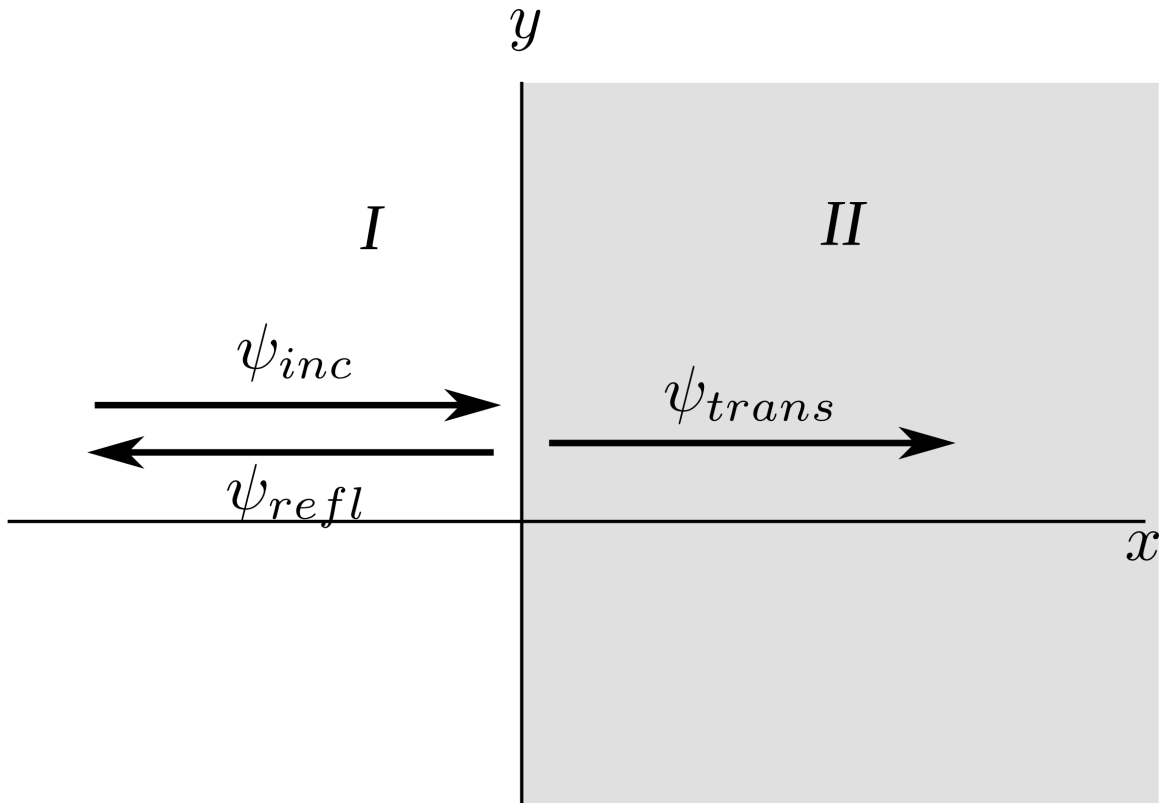


FIG. 3. Transmission and reflection at a stealth material interface is shown. Conditions are determined for making the surface reflection to be zero.

2. *The condition for no reflection at the stealth interfaces*

As the scattered/incoming wave approaches the interface between the propagating region and the stealth boundary, to ensure the wave does not reflect back into the waveguide. We attenuate the wave with a stealth parameter, α , that effectively adds a damping factor to the wave to simulate propagation to infinity. A cubic polynomial is introduced to ensure a smooth transition of the waves stealth parameter.

In 1D let us suppose that we have an interface at $x = 0$ between region I, with no potential, and a region II, with a uniform stealth potential whose strength is to be determined, as shown in Fig. 3. Suppose that electrons are incident on the interface from region I with an amplitude a . We wish to determine the conditions for no reflection from the stealth region; we allow for absorption of the incident waves in region II. This is accomplished by adjusting the material properties of this region.

(i) First let us consider a uniform stealth region. We replace the electron's effective m by

$$\bar{m} = m(1 + i\alpha). \quad (19)$$

Here α is related to the damping factor for the wavefunction in the stealth region. Let the wavefunctions on the two sides be as follows, with the reflected and transmitted amplitudes r and t .

$$\begin{aligned} \psi_I(x) &= a \exp(ik_0x) + r \exp(-ik_0x), \quad x < 0; \\ \psi_{II}(x) &= t \exp[ik_{II}x], \quad x > 0. \end{aligned} \quad (20)$$

The differential equations satisfied by these wavefunctions are

$$\begin{aligned} \frac{d^2}{dx^2} \psi_I(x) + k_0^2 \psi_I(x) &= 0, \quad x < 0; \\ \frac{d}{dx} \frac{1}{\bar{m}/m} \frac{d}{dx} \psi_{II}(x) + k_0^2 \beta \psi_{II}(x) &= 0, \text{ for } x > 0. \end{aligned} \quad (21)$$

The parameter β is chosen below so as to eliminate the reflection from the interface at $x = 0$.

At the boundary $x = 0$, we have the continuity of the wavefunction and of the mass-derivative of the wavefunction, so that

$$\begin{aligned} a + r &= t, \\ i \frac{k_0}{m} (a - r) &= i \frac{k_{II}}{\bar{m}} t. \end{aligned} \quad (22)$$

Hence the ratio of the reflection amplitude to the incident amplitude is

$$\frac{r}{a} = \frac{k_0 \bar{m} - k_{II} m}{k_0 \bar{m} + k_{II} m}, \quad (23)$$

and the condition for no reflection is

$$\bar{m} = \frac{k_{II}}{k_0} m. \quad (24)$$

The wavevector k_{II} in the stealth region is seen to be k_0 multiplied by a complex number, $k_{II} = k_0(1 + i\alpha(x))$, so that the transmitted wave is damped out in that region. The parameter β is now determined by the dispersion relation for region II

$$-\frac{m}{\bar{m}} k_{II}^2 + k_0^2 \beta = 0, \quad (25)$$

leading to $\beta = (1 + i\alpha)$.

(*ii*) We now consider $\alpha(x)$ such that it is a smooth continuous function, increasing as we go further into the stealth region. The differential equation in the stealth region, Eq. (21), is then

$$\frac{d}{dx} \left(\frac{1}{(1 + i\alpha(x))} \frac{d}{dx} \psi_{II}(x) \right) + k_0^2 (1 + i\alpha(x)) \psi_{II}(x) = 0, \text{ for } x > 0, \quad (26)$$

with a solution

$$\psi(x) \sim \exp \left[\pm i k_0 x - k \int_0^{\pm x} \alpha(x') dx' \right]. \quad (27)$$

At any point $x > 0$, we can again consider incident, reflected and transmitted waves in the stealth region. An integration of Eq. (26) across x over a small range from $x - \delta$ to $x + \delta$ yields

$$\frac{1}{1 + i\alpha(x)} \frac{d\psi_{II}(x)}{dx} \Big|_{x-0^+} = \frac{1}{1 + i\alpha(x)} \frac{d\psi_{II}(x)}{dx} \Big|_{x+0^+} \quad (28)$$

showing that the derivative of the wavefunction has a discontinuity that vanishes if $\alpha(x + 0^+) = \alpha(x - 0^+)$. For the same condition, the reflection amplitude also vanishes. In other words, if $\alpha(x)$ is a continuous function we have no reflection throughout the stealth region. Similar conditions for no reflection can be derived for propagation in straight wave guides.

3. Parameter $\alpha(x)$ for the stealth region

The stealth regions, $x_L \leq x \leq x_a$ and $x_b \leq x \leq x_R$, contain no scattering potential or source terms. In these regions we require the electrons to satisfy Schrödinger's equation with a complex mass

$$\bar{m} = m(1 + i\alpha(x)), \quad (29)$$

and a complex wavevector $k = k_0(1 + i\alpha(x))$. We wish to have a smooth transition from the scattering region to the stealth region to avoid reflection of the wave incident on this region. We assume that $\alpha(x)$ is a cubic Hermite interpolation polynomial connecting the value $\alpha = 0$ in the scattering region to a high value at x_L and x_R . The actual maximum value of α is determined by testing out the relation $T = 1$, for Transmission coefficient in the absence of a scattering potential over the range of energies of interest. We note that a choice of α can be made for all energies by replacing $\alpha \rightarrow \alpha/(E/E_0)$, where E_0 is an energy scaling parameter. We have not done so in the calculations presented here. The maximum value of α was $100/2\pi$ in the following 1D calculations.

To determine the choice of α when we moved on to the case of scattering in a waveguide, we tested various values of α to see which one completely absorbs the transmitted and reflected wave, thereby giving the most accurate results. Figure 4 shows how the R+T coefficient varies as a function of stealth parameter, α . We compared the R+T line with a line with a y-coordinate of 1. The value of α that had R+T closest to 1 was chosen for the scattering calculation.

C. Results for 1D tunneling in a double barrier resonant tunneling structure

We consider a double barrier resonant tunneling structure with barriers of GaAlAs of thickness 100\AA enclosing a well region of 100\AA . The barrier height was chosen to be 0.3 eV, and the effective mass $m = 0.067m_0$ corresponding to the conduction band effective mass in GaAs, was used in the calculations. The geometry is shown in Fig. 5, with the location of the source and the stealth regions on either end of the active region. The stealth parameter, $\alpha(x)$, is specified by a cubic Hermite interpolation polynomial. In Fig. 6, we show the incident wave moving to the right of the source. The wave emanating from the source towards the $-x$ -direction does not affect the scattering in the “active region,” and is

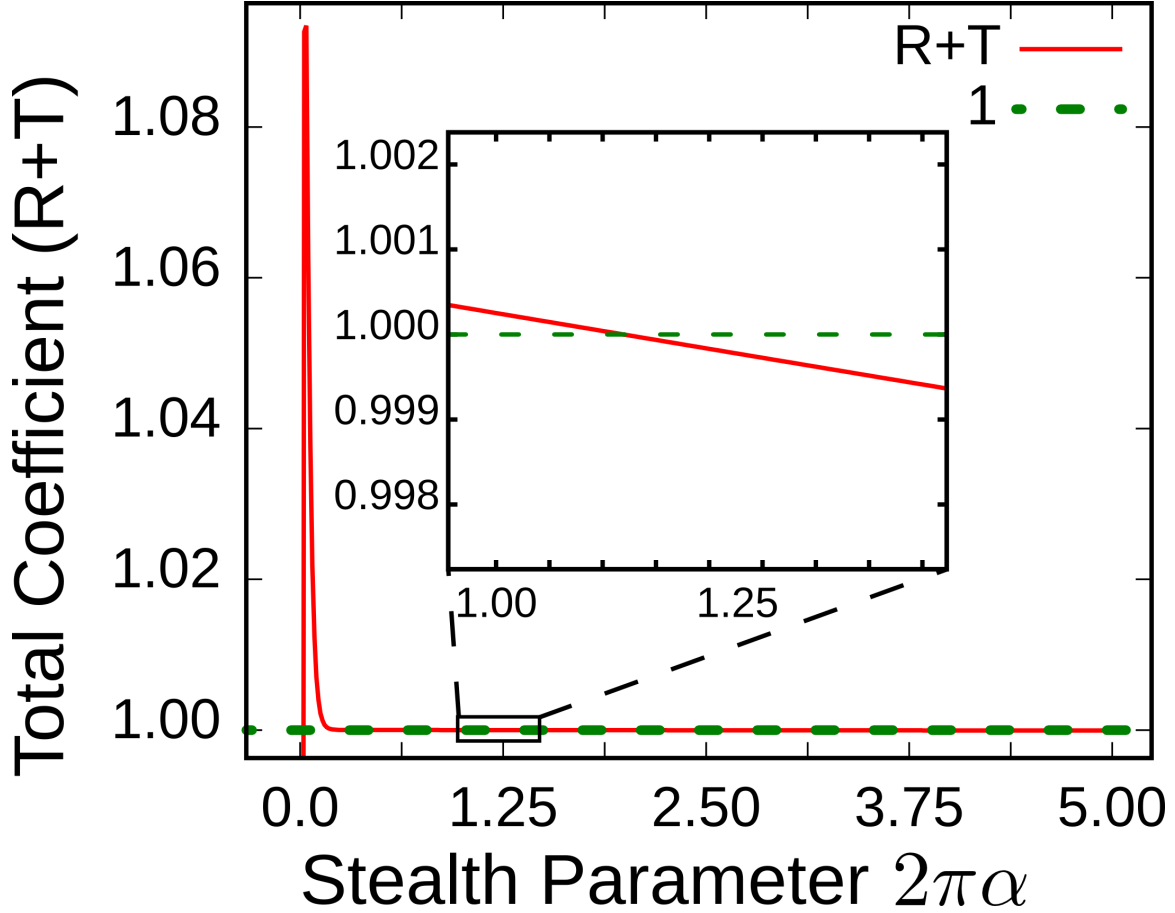


FIG. 4. A plot of the sum of reflection plus transmission coefficient as a function of stealth parameter α is shown. This plot shows the variation of R+T and what values of α give accurate results. The value α which made R+T closest to 1 was chosen for our calculations.

absorbed in the stealth region on the left. One of the above-barrier localized wavefunction is also shown. The transmission coefficient for the structure is shown in Fig. 7, including the resonant peaks due to the above-barrier localized states.

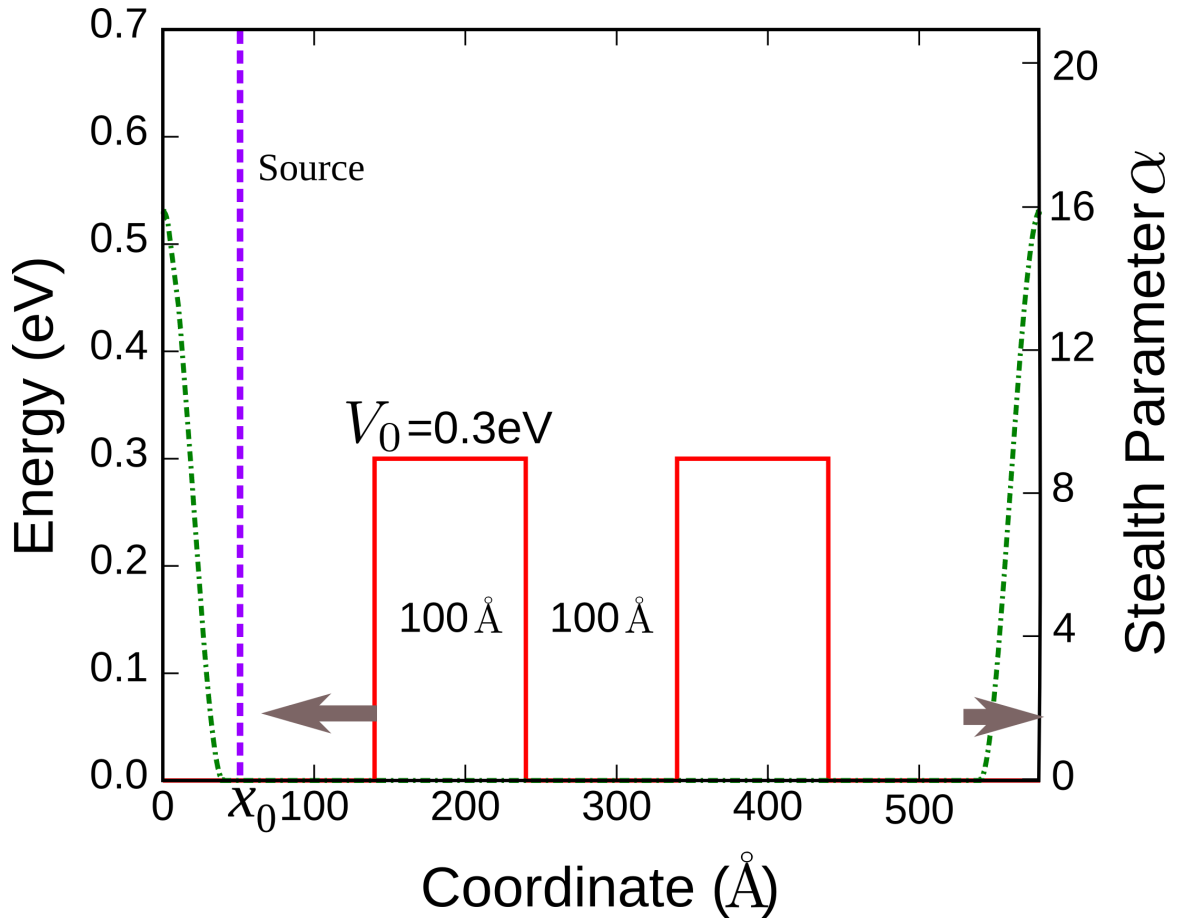


FIG. 5. A double barrier structure with 100 \AA barriers and 100 \AA well region is shown. The stealth region is shown (dash-dot curve) where the parameter α is not zero. It has been assumed to be a cubic in order to provide a smooth barrier for absorption. The carrier effective mass corresponds to the electron mass in the conduction band of GaAs. The source is located at x_0 and is represented as a dashed line.

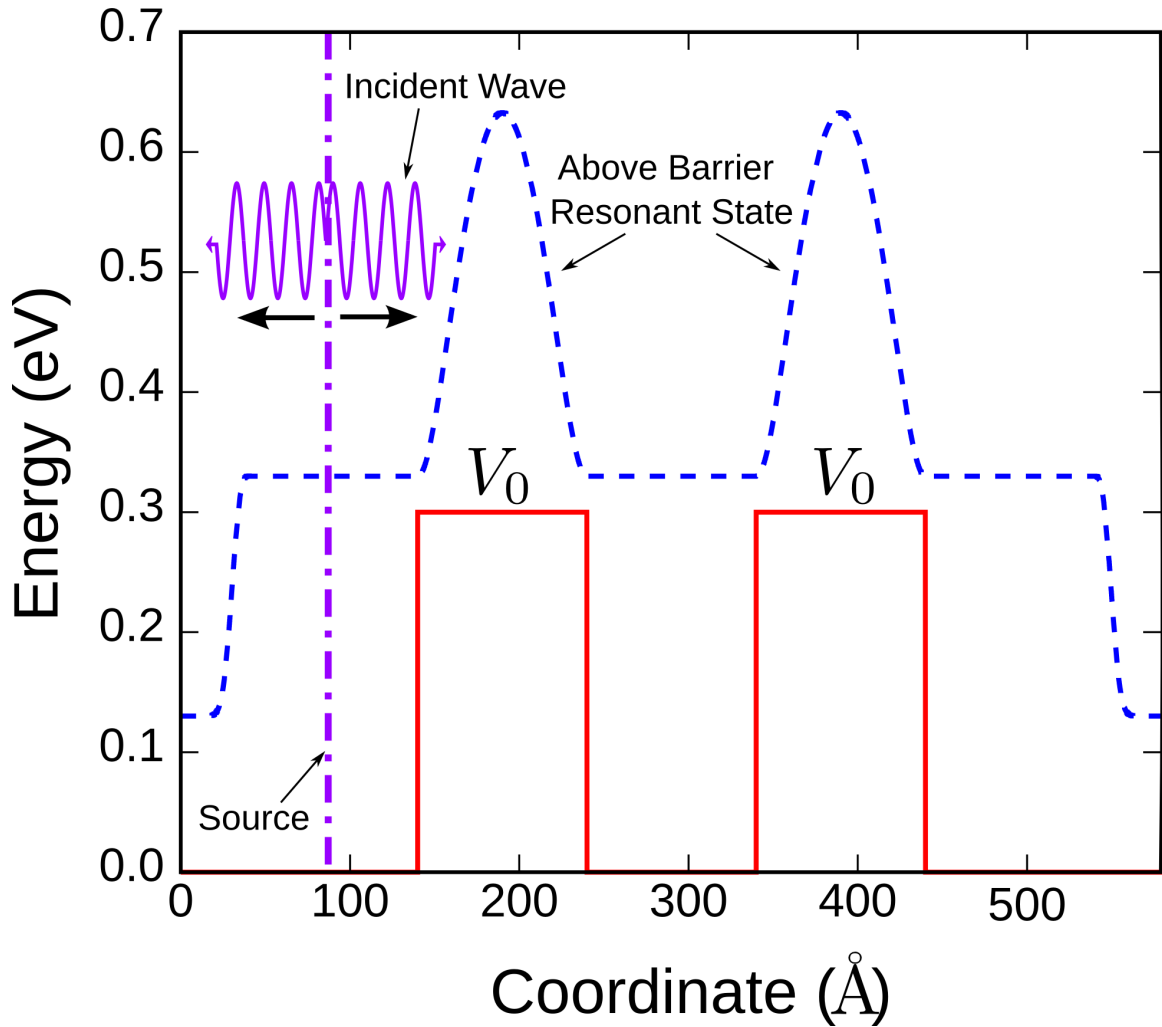


FIG. 6. The source is shown as a vertical (dash-dot) line with waves moving to the right as well as the left from it. The potential profile of a double barrier structure with 100\AA barriers of height 300 meV and a well of width 100\AA is shown. The probability density (dashed curve) of an above-barrier resonant state localized above the barriers is shown, with it dropping to zero in the stealth region. The curve has been shifted upwards to suggest that its energy is above the barrier.

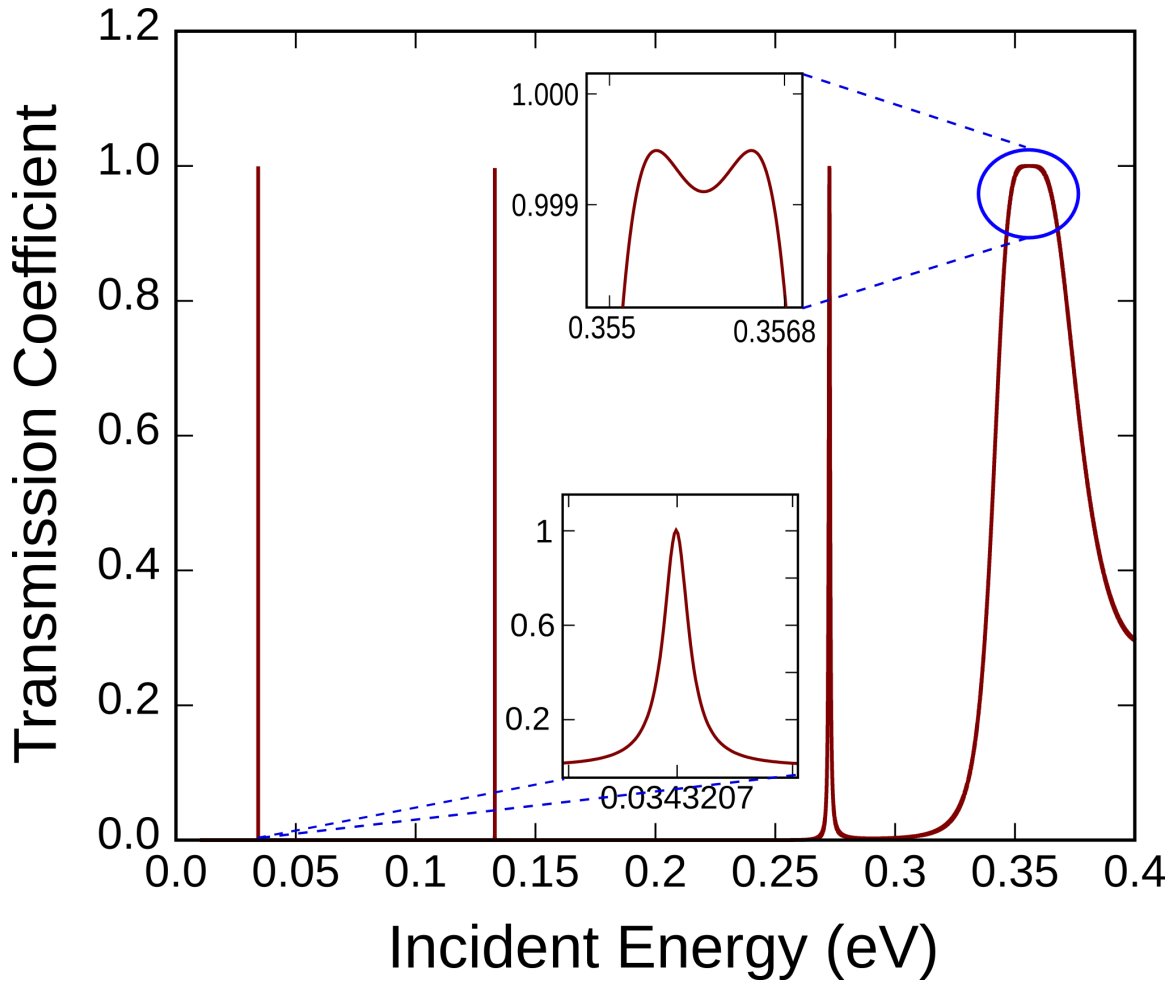


FIG. 7. The resonances observed for a potential profile of a double barrier structure with 100\AA barriers of height 300 meV and a well of width 100\AA are shown. Two insets are shown, one for the lowest resonant state at 0.034 meV and the other for the nearly degenerate above-barrier resonances at $\sim 0.355\text{ eV}$.

III. 2D SCATTERING AND STEALTH FINITE ELEMENTS

A. Action Integral and Stealth Parameters in the Waveguide

In a waveguide of width L , the potential energy in the launch and detection regions away from the scattering center are taken to be

$$V(x, y) = \begin{cases} 0, & 0 \leq y \leq L, \\ \infty, & y < 0 \text{ or } y > L \end{cases} \quad (30)$$

In these regions Schrödinger's equation is separable with

$$\phi(x, y) = \sum_{n=1} \psi_n(y) (a_n e^{ik_n x} + r_n e^{-ik_n x}), \quad (31)$$

where

$$\psi_n(y) = \sqrt{\frac{2}{L}} \sin\left(\frac{n\pi y}{L}\right) \quad (32)$$

In effect the motion of carriers can be represented as a quasi-1D wave propagation and these correspond to the prepared initial state at $x = x_0$. The action integral for the steady state problem is given by

$$A/T = \int_0^{L_y} dy \int_{x_a}^{x_b} dx \phi^*(x, y) \left[\overleftarrow{\nabla} \frac{\hbar^2}{2m} \overrightarrow{\nabla} - E \right] \phi(x, y). \quad (33)$$

in the region free of any scattering potential.

1. Source Term in a 2D waveguide

As in the 1D case, we will require a source term close to the active region so that an incident wave can be launched in the 2D waveguide once absorbing regions are employed to simplify the BCs. Let us suppose that in the region with the source term there is no potential, and the waveguide has width L along transverse direction, y . Then we use a variant on the 1D derivation of the source term. The Schrödinger equation in this region becomes

$$-\frac{\hbar^2}{2m} \nabla^2 \psi = E\psi. \quad (34)$$

We want to add a source term $-\hbar^2/(2m)S\delta(x - x_0)$, which will generate plane waves of the form

$$\psi(x, y) = A \exp(ik_x|x - x_0|)\phi(y), \quad (35)$$

where $\phi(y)$ is a superposition of the bound states of the infinite well of length L . Now, we add the source term to the right hand side of Eq. (34) and substitute ψ from Eq. (35) to get

$$-\frac{\hbar^2}{2m}S\delta(x - x_0) = -\frac{\hbar^2}{2m}\nabla^2\psi - E\psi \quad (36)$$

$$S\delta(x - x_0) = \left(\frac{\partial^2}{\partial x^2} + \frac{\partial^2}{\partial y^2} + k_0^2 \right) \psi(x, y) \quad (37)$$

$$S\delta(x - x_0) = \left(\frac{\partial^2}{\partial x^2} - k_y^2 + k_0^2 \right) \psi(x, y), \quad (38)$$

Integrating both sides over $x = x_0$ we have

$$S = \lim_{\epsilon \rightarrow 0} \int_{x_0-\epsilon}^{x_0+\epsilon} dx \left(\frac{\partial^2}{\partial x^2} - k_y^2 + k_0^2 \right) \psi(x, y) \quad (39)$$

$$S = \lim_{\epsilon \rightarrow 0} \frac{\partial}{\partial x} A \exp(ik_x|x - x_0|)\phi(y) \Big|_{x_0-\epsilon_0}^{x_0+\epsilon_0} \quad (40)$$

$$S = 2Aik_x\phi(y). \quad (41)$$

Where $k_y^2 = n^2\pi^2/2mL^2$ and $k_0^2 - k_y^2 = k_x^2$. The form of the source term in 2D is analogous to its 1D counterpart with the addition of the $\phi(y)$ term.

B. Double quantum barrier in a waveguide

As proof-of-concept, we compare scattering off a double Quantum barrier in 1D to scattering off the same barrier in a 2D waveguide with the barriers extending fully across the waveguide. The mesh used for this model is shown in Fig. 8. Since the potential barrier extends along the entire waveguide, the Schrödinger equation describing the scattering of both the double and single quantum barrier are separable in the $x -$ and $y -$ directions. Due to this, the solution in the $y -$ direction will only add a transverse energy to the total energy, meaning that the plot of transmission coefficient vs energy will have the same shape. The only difference should be that in the 2D case the plot is shifted by the energy of the incident mode in the transverse direction. This can be seen in Fig. 9. As a result of the

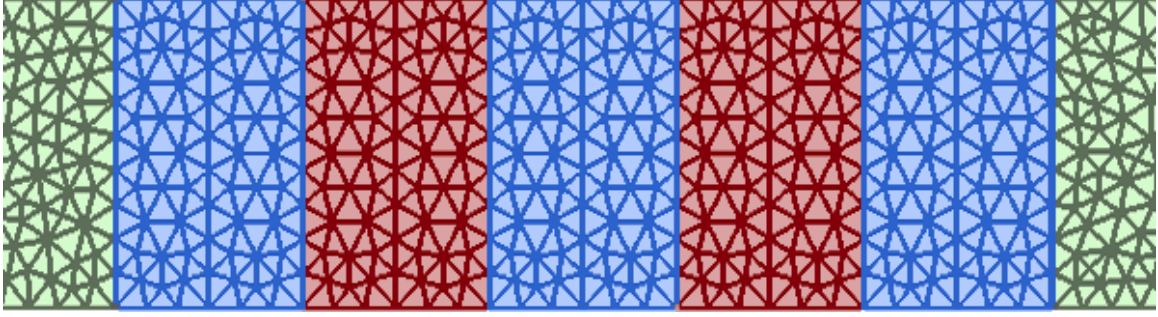


FIG. 8. The mesh used for the FEM calculation of the double quantum barrier in a waveguide is shown. The scattering centers are in red, the stealth region is in grey, and the propagation region is in blue.

waveguide confining the electron in the transverse direction, we get the solution, in the y direction, of the infinite potential well. Thus the total incident energy, E_{inc} , is the sum of the energy in the x - direction and y - direction, such that

$$E_{inc} = E_x + E_y \quad (42)$$

$$E_{inc} = E_x + \frac{\hbar^2 n^2 \pi^2}{2m^* L^2} \quad (43)$$

Additionally, with the finite element method, the wavefunction for the below barrier resonances can be obtained in the same manner as in the 1D case. The wavefunction for an incident wave with transverse mode $n=3$ in the second below barrier resonant state is shown in Fig. 10 and Fig. 11. The above barrier resonant states can be obtained as well, the first two are shown in Fig. 12 and Fig. 13.

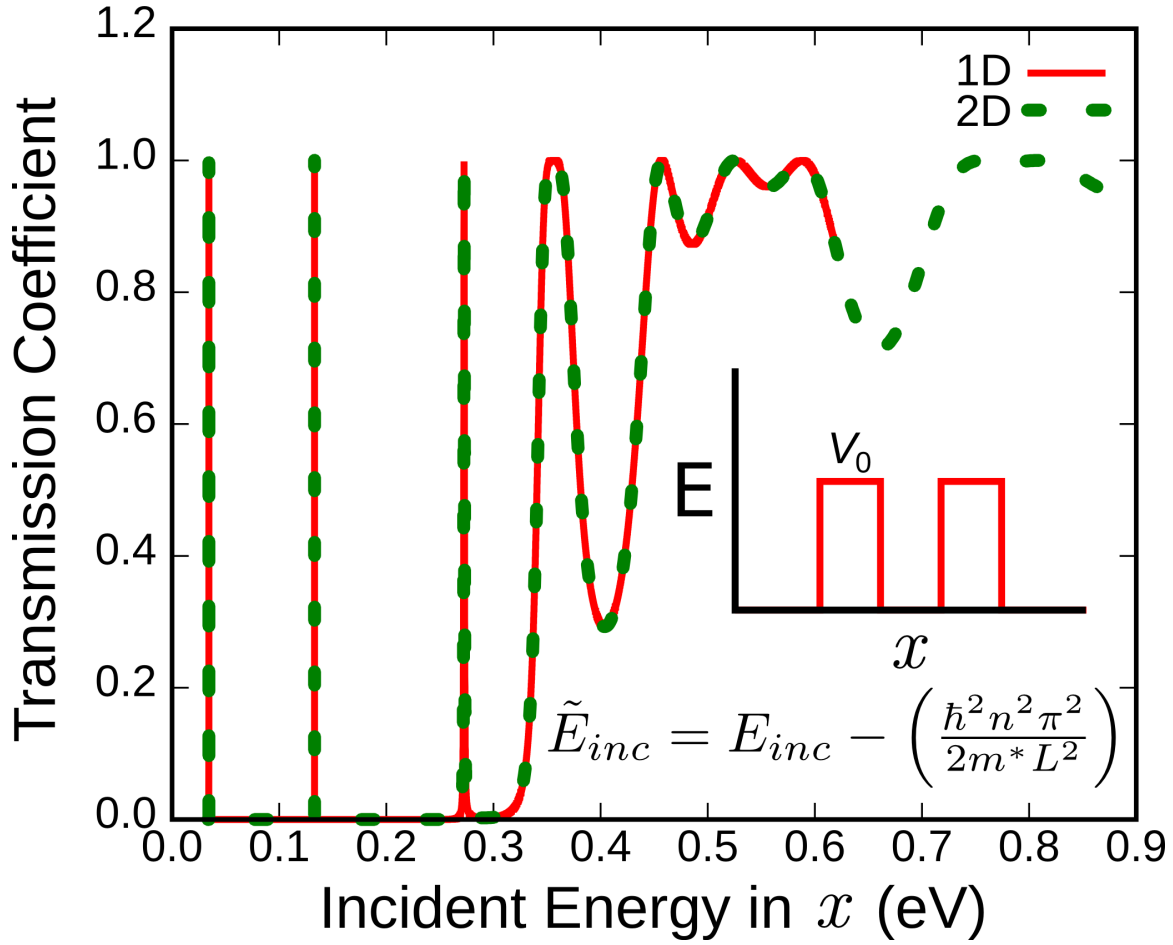


FIG. 9. The plot of transmission coefficient as a function of energy for the 1D double barrier and the 2D double barrier are shown. We see that the transmission coefficients in the 2D transmission coefficient is shifted by the energy identical with the shifted energy used for 2D. This verifies the separability of the Schrödinger equation for the waveguide.

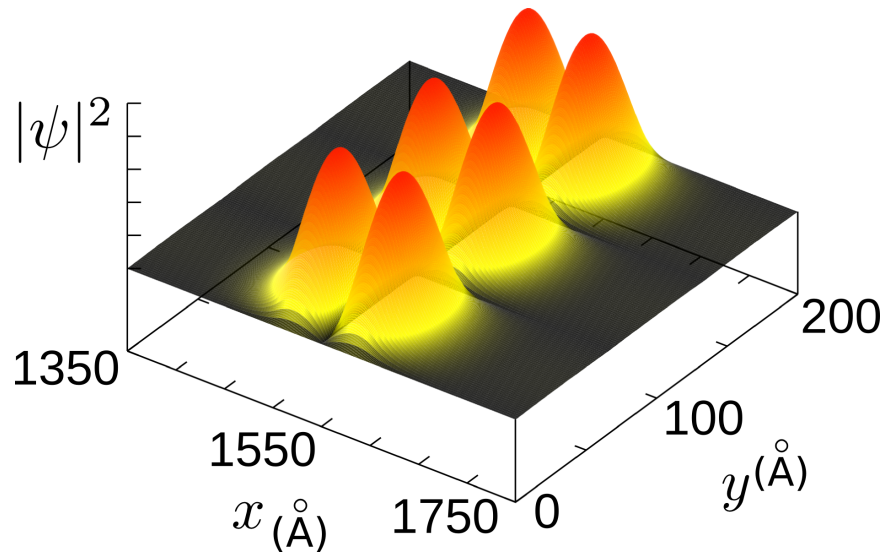


FIG. 10. Plot of the wave function for the second below barrier resonant state of the double barrier is shown. The wavefunction is confined between the two barriers and has even symmetry.

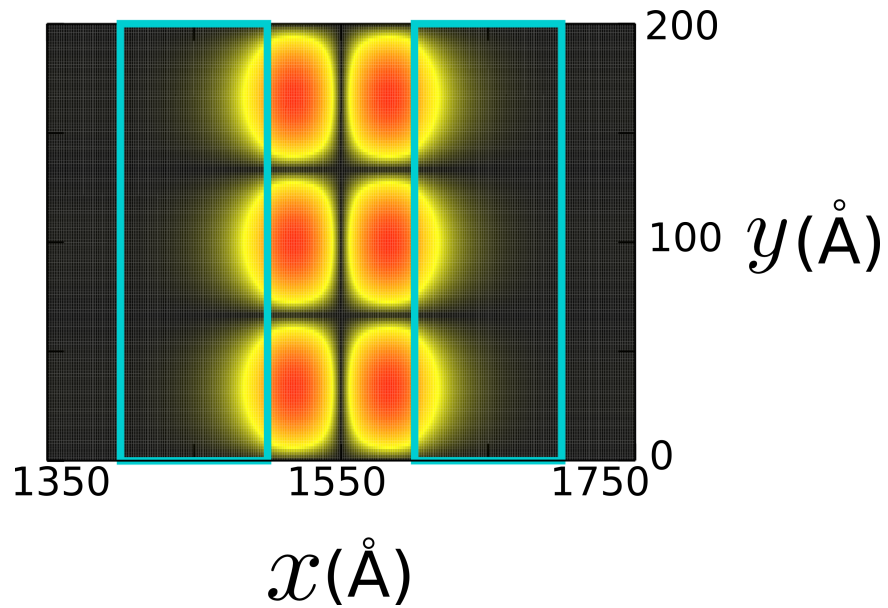


FIG. 11. Top-down view of the same wavefunction.

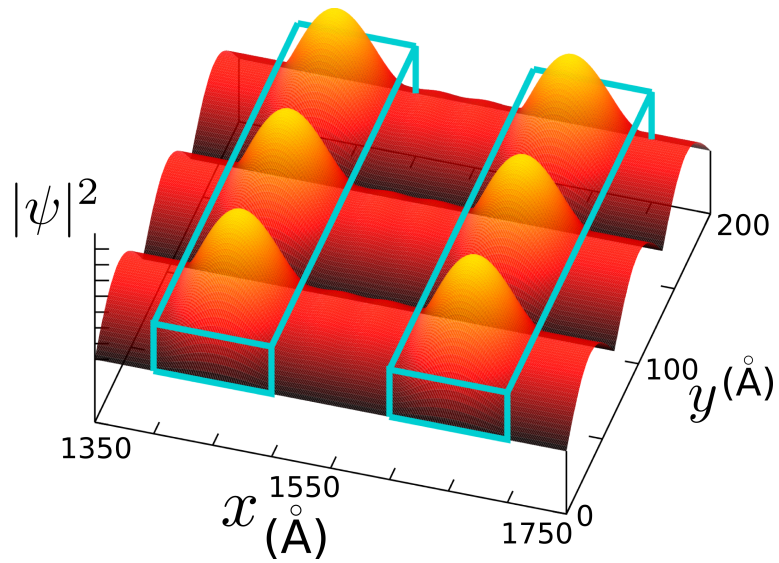


FIG. 12. The first above barrier resonant state is shown. The wavefunction here is even, so there is constructive interference between the barriers.

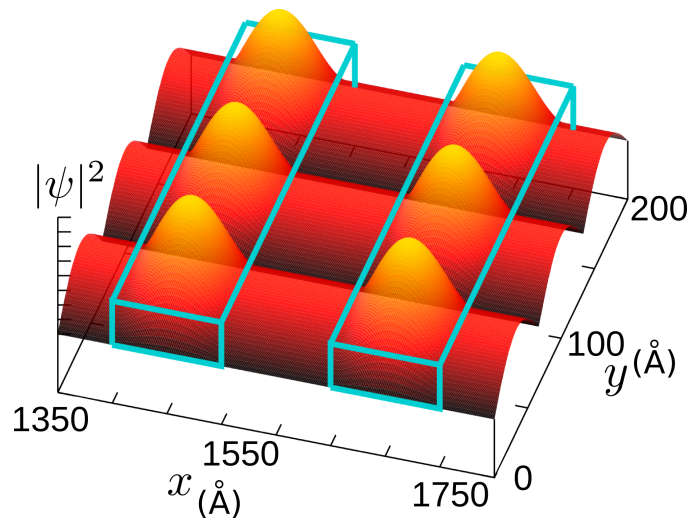


FIG. 13. The second above barrier resonant state is shown. The wavefunction here is odd, so there is destructive interference between the barriers.

C. Modal decomposition of wavefunction

It has been shown by Bagwell¹³ that near the scattering center, evanescent modes exist. Scattering calculations in textbooks employ asymptotic boundary conditions, which calculate the scattered wave at infinity. In the asymptotic region, the evanescent modes have diminished and are not accounted for. Also, these evanescent modes do not contribute to the probability current in any region, asymptotic or finite. The finite element method allows contributions from these evanescent waves to be calculated. We do this by performing a Fourier decomposition of the wavefunction obtained.

The transmission and reflection coefficient are calculated from the probability current density, \mathbb{J} , given by the form,

$$\mathbb{J} = \frac{\hbar}{2m^*i} \left(\psi^* \frac{\partial \psi}{\partial x} - \psi \frac{\partial \psi^*}{\partial x} \right). \quad (44)$$

We can find R and T from this by

$$R = \frac{\mathbb{J}_{\text{refl}}}{\mathbb{J}_{\text{inc}}} \quad (45)$$

$$T = \frac{\mathbb{J}_{\text{trans}}}{\mathbb{J}_{\text{inc}}} \quad (46)$$

where the subscripts represent reflected, incident and transmitted waves. We also know that propagating waves are of the form

$$\psi(x, y) = Ae^{ik_x|x-x_0|} \sin(k_y y) \quad (47)$$

and evanescent waves are of the form

$$\psi(x, y) = Ae^{\kappa|x-x_0|} \sin(k_y y) \quad (48)$$

where, κ , is the evanescent wavevector given by

$$\kappa = \frac{\sqrt{2m^*(V - E)}}{\hbar}. \quad (49)$$

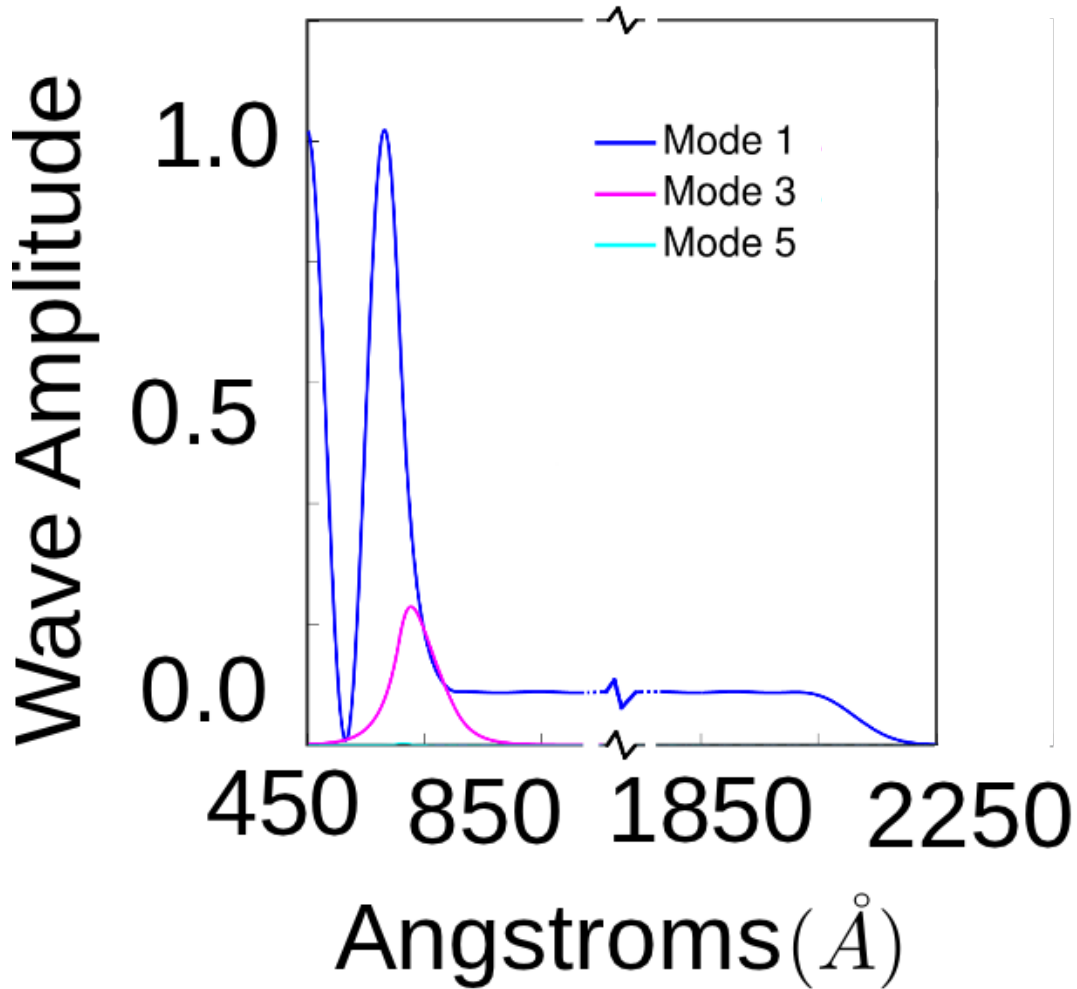


FIG. 14. This plot shows the modulus squared of the Fourier coefficients as a function of distance in the waveguide. The non-evanescent mode, mode 1, propagates through the waveguide without any decay. However mode 3 and mode 5 are evanescent modes which decay very rapidly. Here we can see that after a few hundred angstroms when the wave moves past the scatterer, the evanescent modes have diminished. The large oscillation on the left hand side of the figure is the portion of the wave that has been reflected from the scatterer.

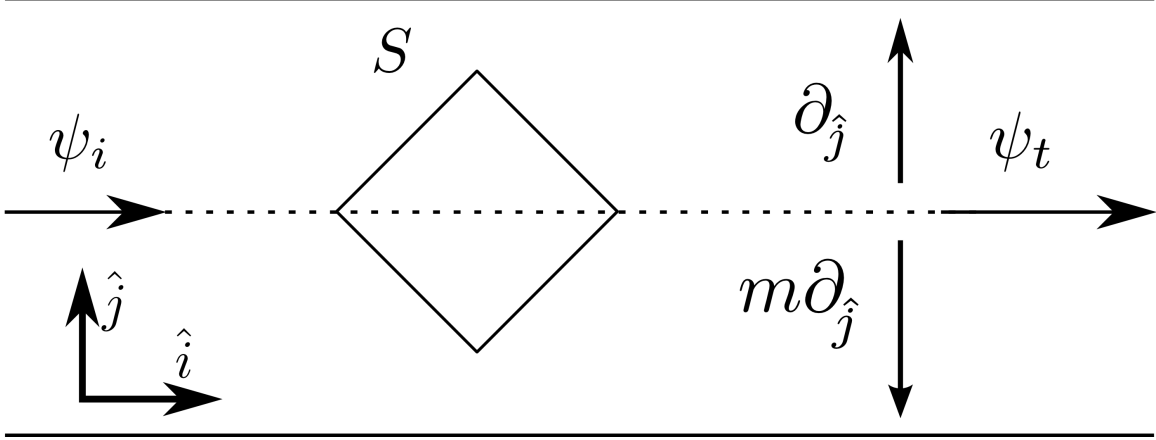


FIG. 15. The figure of a bilaterally symmetric wavefunction scatterer, S , in a bilaterally symmetry waveguide. We have that ψ_i is the incoming wavefunction, ψ_t is the transmitted wavefunction, ∂_{e_2} is the operator in the respective cartesian direction.

D_1	ϵ	m
R_+	1	1
R_-	1	-1

TABLE I. Character Table for the dihedral group of order two, D_1 , is shown.

D. Scattering from a bilateral symmetric potential in a waveguide

Let us consider an incident plane wave in a waveguide, ψ_i , scattering off a potential, S , which results in a scattered wavefunction ψ_t . If ψ_i approaches S , a quantum barrier, well or both, with a trajectory such that S has bilateral symmetry, then we can ask how the symmetry of ψ_t is determined by the symmetries of ψ_i and S , as shown in Fig. (15).

The bilateral symmetry group is also called D_1 , the dihedral group of order two. The group is made of the identity, ϵ , and mirror, m , operations, and two irreducible representations. The character table is shown in Table I The transmitted wavefunction is approximately determined by the application of the Hamiltonian $H = (\partial^2 + S)$ on the incident wavefunction ψ_i . Where the factor of $(-\hbar^2/2m)$ has been factored into ∂^2 since we are only concerned

with the symmetry of the operator. Then ψ_t must have a symmetry determined by

$$R(\psi_t) = R(\partial^2 + S) \otimes R(\psi_i) \quad (50)$$

$$= [R(\partial^2) + R(S)] \otimes R(\psi_i) \quad (51)$$

The symmetry of ∂^2 that is of interest here has only to do with the component of ∂^2 orthogonal to the mirror line. As seen in Fig. 15, the vector ∂_j transforms according to the irreducible representation R_- , since $\epsilon\partial_j = \partial_j$, and $m\partial_j = -\partial_j$. The irreducible representation of ∂_j^2 can be calculated from that of ∂_j through the characters of the direct product of

$$\chi(\partial_j^2)(C_i) = [\chi(\partial_j)(C_i)] * [\chi(\partial_j)(C_i)] \quad (52)$$

where χ stands for character and C_i stands for an operation in class i . Thus

$$\chi(\partial_j^2)(\epsilon) = 1 * 1 = 1, \quad \text{and} \quad (53)$$

$$\chi(\partial_j^2)(m) = (-1) * (-1) = 1, \quad \text{so} \quad (54)$$

$$R(\partial_j^2) = R_+ \quad (55)$$

Combining Eq. 51 and Eq. 55 we get,

$$\chi(\psi_t)(C_i) = [\chi(\partial_j^2)(C_i) + \chi(S)(C_i)] * \chi(\psi_i)(C_i) \quad (56)$$

$$= [\chi(R_+)(C_i) + \chi(S)(C_i)] * \chi(\psi_i)(C_i) \quad (57)$$

With Eq. 57 we can analyze the following situations.

In the first case we have that the scatterer is symmetric about the mirror plane, and the incident wave function is symmetric about that same plane, then we can say

$$R(S) = R_+ \quad (58)$$

$$R(\psi_i) = R_+ \quad (59)$$

$$R(\psi_t) = (R_+ \oplus R_+) \otimes R_+ = 2R_+ \quad (60)$$

The factor of two in the $R(\psi_t)$ tells us that there will be two modes both of symmetry R_+ . Since we are ignoring one of the dimensions of the problem this analysis is only approximate, so we should make the less specific claim that there will be more modes in ψ_t than in ψ_i , all of the same symmetry.

In the second case we have an antisymmetric incident wave scattering off a symmetric scatterer. We have

$$R(S) = R_+ \tag{61}$$

$$R(\psi_i) = R_- \tag{62}$$

$$R(\psi_t) = (R_+ \oplus R_+) \otimes R_- = 2R_- \tag{63}$$

Again ψ_t has the same symmetry as ψ_i , but with more modes.

Now consider a scattering potential that has R_- symmetry. Such a potential could be realized by having a barrier on one side of the mirror plane with a potential well on the other side of the mirror plane. We then obtain

$$R(S) = R_- \tag{64}$$

$$R(\psi_i) = R_- \tag{65}$$

$$R(\psi_t) = (R_+ \oplus R_-) \otimes R_- = R_- \oplus R_+ \tag{66}$$

$$R(S) = R_- \tag{67}$$

$$R(\psi_i) = R_+ \tag{68}$$

$$R(\psi_t) = (R_+ \oplus R_-) \otimes R_+ = R_+ \oplus R_- \tag{69}$$

Thus for an antisymmetric scattering potential, the transmitted wavefunction will have modes of both parity no matter what the parity of the incident wavefunction is.

E. Arbitrary shapes for scattering potentials: circle and square

In the case of a scattering potential that does not extend across the entire waveguide, we still have a transverse energy present in the incident wave; however it cannot be easily separated. Thus for an antisymmetric scattering potential, the transmitted wavefunction will have modes of both parity no matter the parity of the incident wave function. from the action integral. Also, there is no one-dimensional analogy for the finite width arbitrary scattering center, so we cannot easily predict or compare the results, as was done before in the previous section for the double quantum barrier. Here the cases for both the circle and square are presented, due to similar types of symmetry. The square and circle are

both present in a 300 \AA waveguide. The square has sides of 100 \AA , while the circle has a diameter of 100 \AA . Both scatterers have a barrier height of 300 meV . They are placed in the center of the waveguide such that the configuration is symmetric. The meshes used for their calculations are shown in Fig. 16 and Fig. 17.

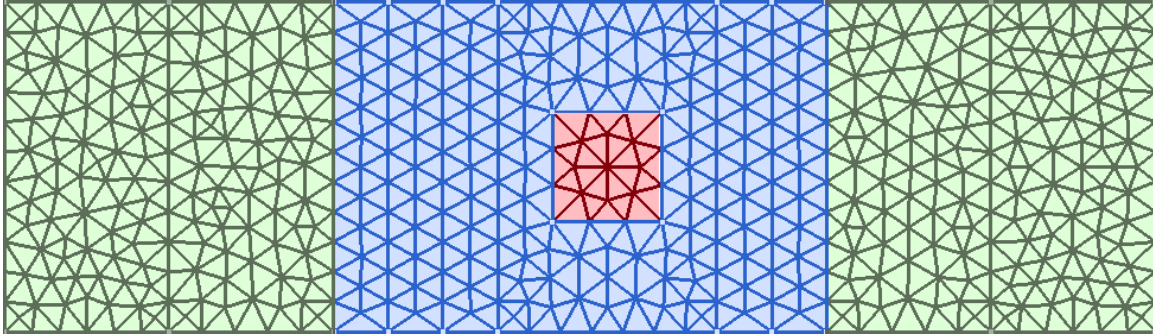


FIG. 16. The mesh used for the FEM calculation of the square scattering center in a waveguide is shown. The scattering center is in red, the stealth region is in grey, and the propagation region is in blue.

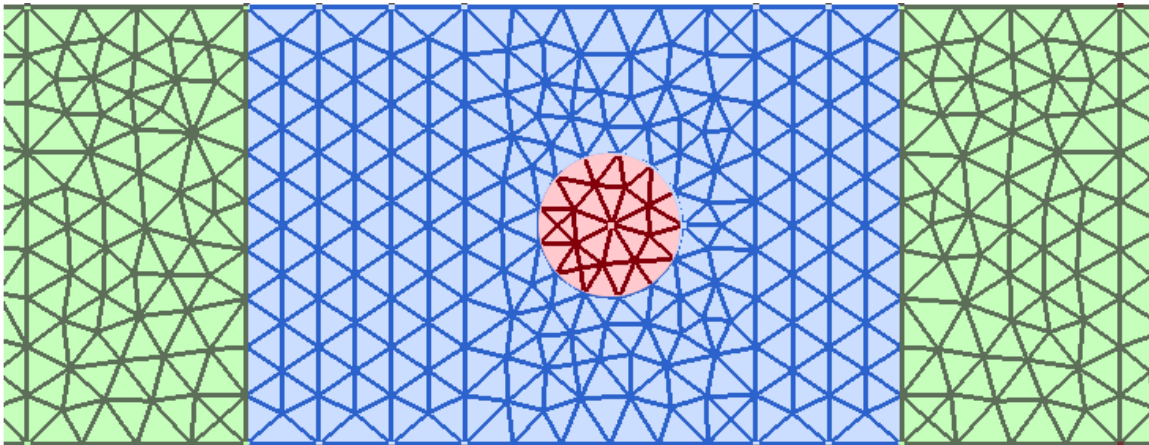


FIG. 17. The mesh used for the FEM calculation of the circle scattering center in a waveguide is shown. The scattering center is in red, the stealth region is in grey, and the propagation region is in blue.

In this case we exhibit a modal decomposition, using Fourier decomposition of the solved wavefunction, obtained through our calculation. This allows us to examine the individual modal contributions to the probability current and transmission/reflection coefficients. Using the decomposed wavefunction, we can see when new channels in the waveguide are

opened, since we can plot each mode individually. Another indication of a channel opening is the rapid oscillations in the T vs. E plot at the thresholds. Thus shown in Fig. 18, these thresholds are indicated by dashed vertical lines, which correspond to the threshold energy levels. These rapid oscillations are not due to numerical error because we can see that, except for low energies, the $R+T$ is essentially unity, in agreement with scattering theory and conservation of energy. First we show the T vs. E plots for the square case.

Various incident modes have been examined, up to $n = 4$. In the case of odd transverse modes, we do not see any even modes present in the waveguide, as seen in Fig. 18. This is due to the symmetry of the mode being preserved. In the case when an even mode is injected into the waveguide, we see that only the even modes are present. The differences between the square and the circle are minor, due to the different types of symmetry for them; however the T vs. E plots for the two cases are different.

An interesting observation is that when we introduce an even mode into the waveguide with a circular scatterer, the T vs. E plot resembles that of a lens scatterer. This can be seen that Fig. 21 and Fig. 43. This is because the $n=2$ mode makes the circular scatterer resemble a lens.

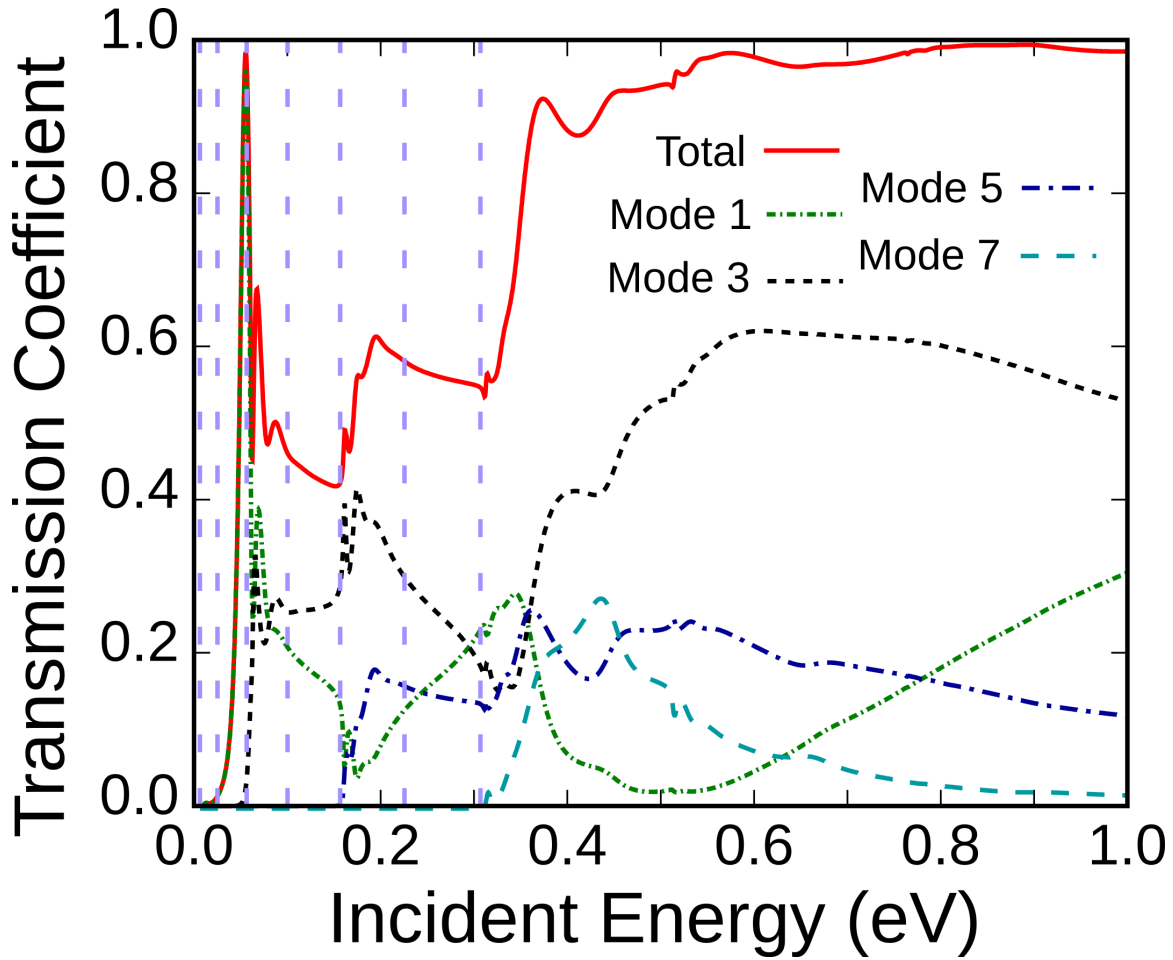


FIG. 18. The incident transmission versus energy plot for the square scatterer, with an incident plane wave in mode $n=1$ is shown. Here we can see contribution from only odd modes due to the symmetry of the incident mode being preserved by the bilaterally symmetric square scatterer in the waveguide. The thresholds for each transmitted mode correspond to new a channel being opened. These thresholds are indicated by the vertical dashed lines.

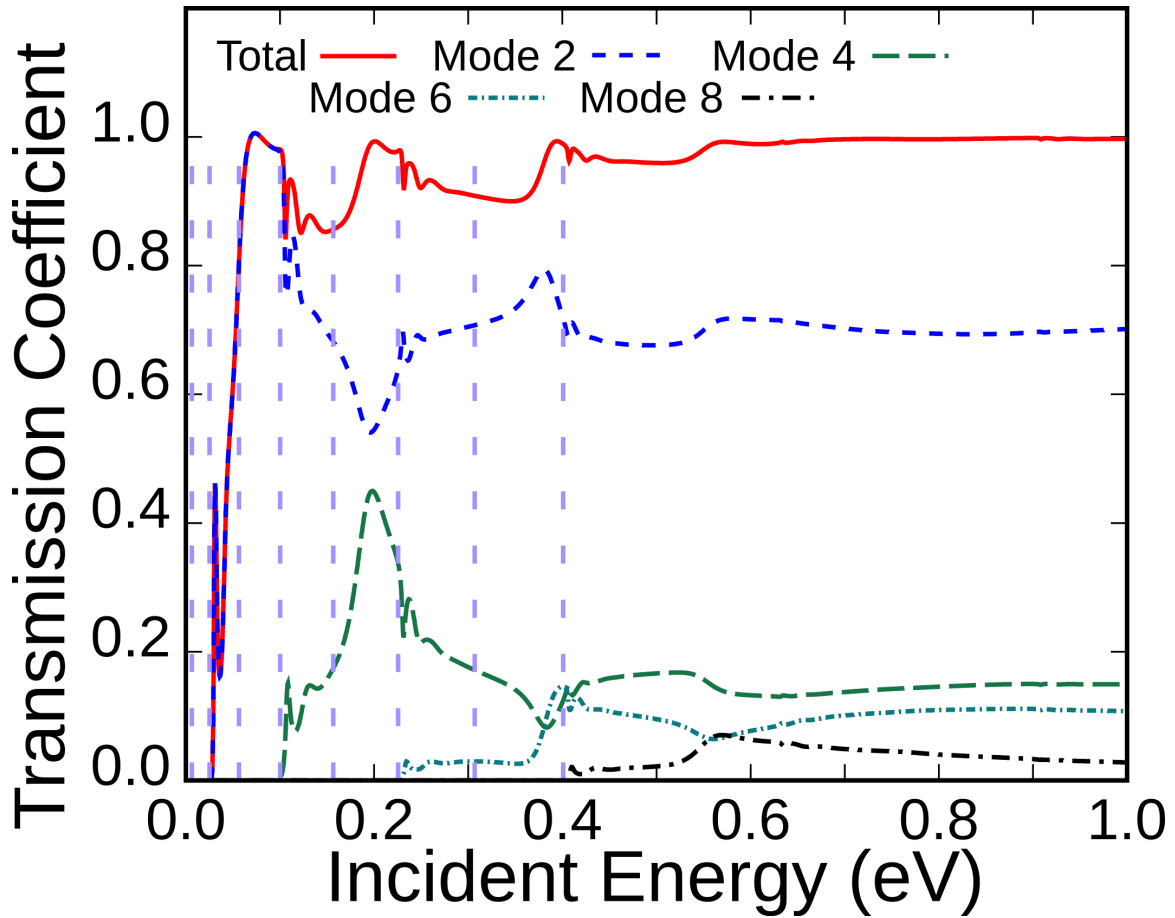


FIG. 19. The incident transmission versus energy plot for the square scatterer, with an incident plane wave in mode $n=2$ is shown. Here we can see contribution from only even modes due to the symmetry of the incident mode being preserved by the bilaterally symmetric square scatterer in the waveguide. The thresholds for each transmitted mode correspond to new a channel being opened. These thresholds are indicated by the vertical dashed lines.

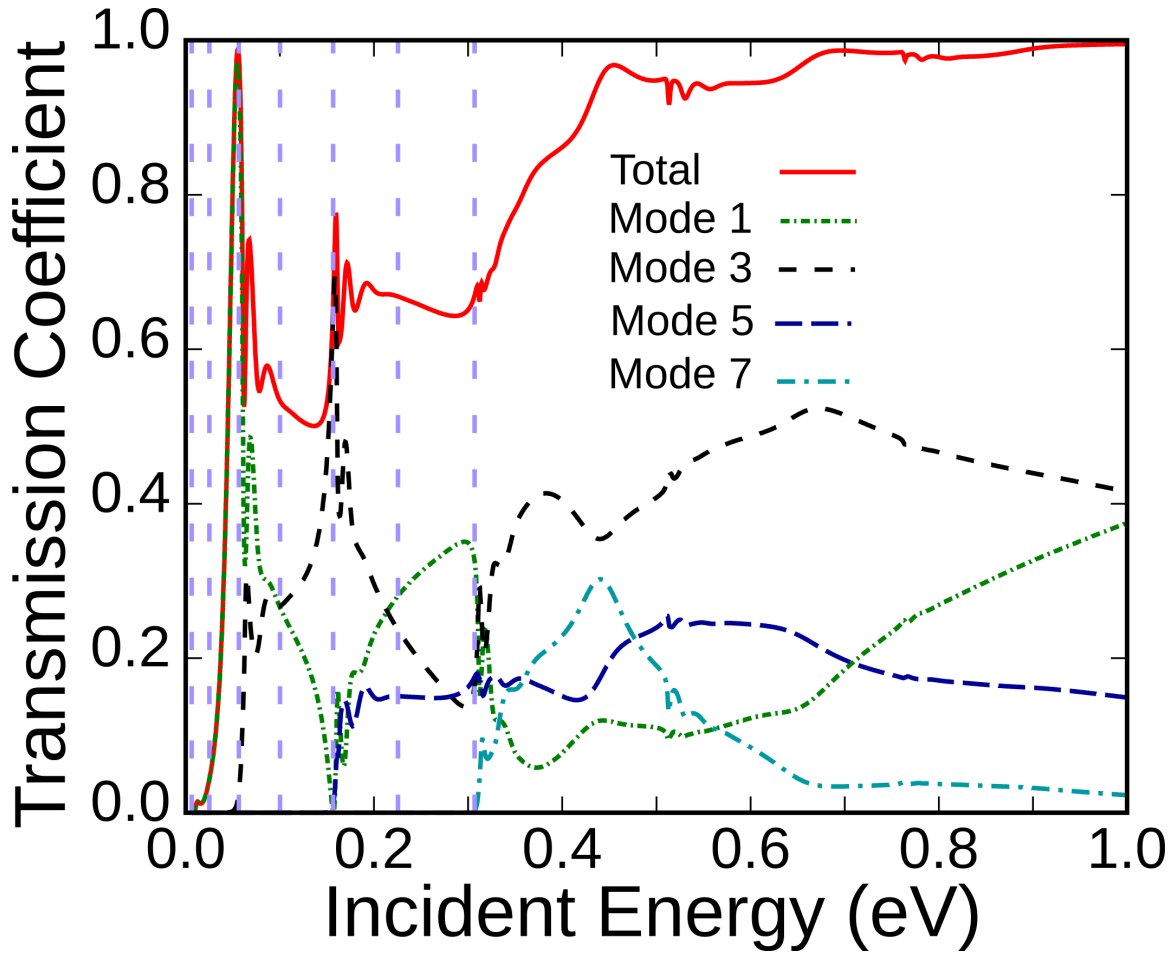


FIG. 20. The incident transmission versus energy plot for the circular scatterer, with an incident plane wave in mode $n=1$ is shown. Here we can see contribution from only odd modes due to the symmetry of the incident mode being preserved by the bilaterally symmetric square scatterer in the waveguide. The thresholds for each transmitted mode correspond to new a channel being opened. These thresholds are indicated by the vertical dashed lines.

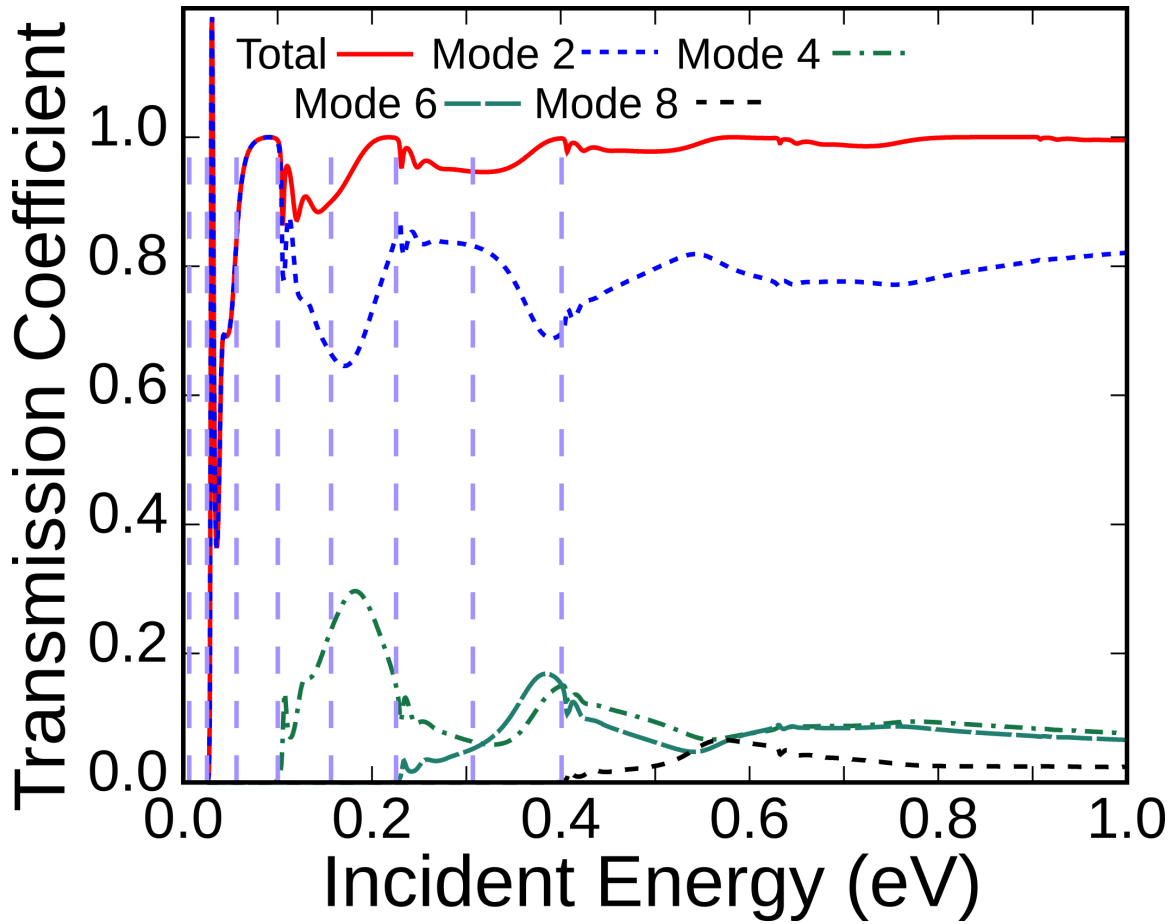


FIG. 21. The incident transmission versus energy plot for the circular scatterer, with an incident plane wave in mode $n=2$ is shown. Here we can see contribution from only even modes due to the symmetry of the incident mode being preserved by the bilaterally symmetric square scatterer in the waveguide. The thresholds for each transmitted mode correspond to new a channel being opened. These thresholds are indicated by the vertical dashed lines.

F. Arbitrary scattering potential: lens

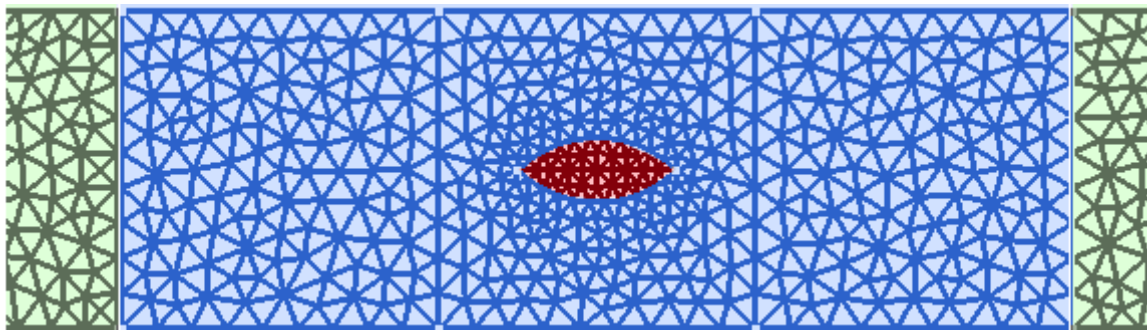


FIG. 22. The mesh used for the FEM calculation of the lens scattering center in a waveguide. The scattering center is in red, the stealth region is in grey, and the propagation region is in blue. We rotated the lens scatterer in increments of 45 degrees.

The lens is another type of scattering center that can have interesting scattering effects. Here different rotations of the lens have been examined to inspect the different effects of lens orientation. The first orientation examined is the zero (or 180) degree orientation of the lens scatterer.

The transmission versus energy plot for different incident modes are shown in Figs. 23, 43, 44, and 45. An obvious pattern to notice is that when an odd mode is incident, only odd modes are present in the waveguide. When an even mode is incident, only even modes contribute. Another thing to notice is that when $n=2$ is incident, mode 2 has a large presence in the waveguide while the other modes do not. This happens when an odd mode is incident, but not as drastically as in the case of an even incident mode.

Next, the transmission versus energy plot for a rotation of 90 degrees, same as a 270 degree rotation, is shown in Fig. 24, 46 47, and 48 Since more of the scatterer is exposed to the incident wave in the x-direction, more interesting Energy versus Transmission plots are produced. The same kind of symmetry where odd incident modes produce only odd modes in the waveguide, and likewise for even incident modes, occurs here as well.

In the case of a 45 degree rotation, we get the same results as if the lens were rotated 135, 225, and 315 degrees. Every mode is present in the waveguide due to the rotation of the lens causing a break in the even and odd symmetry. However, it is easily seen that when a certain mode is incident, that mode is the most dominant contributor to the wavefunction.

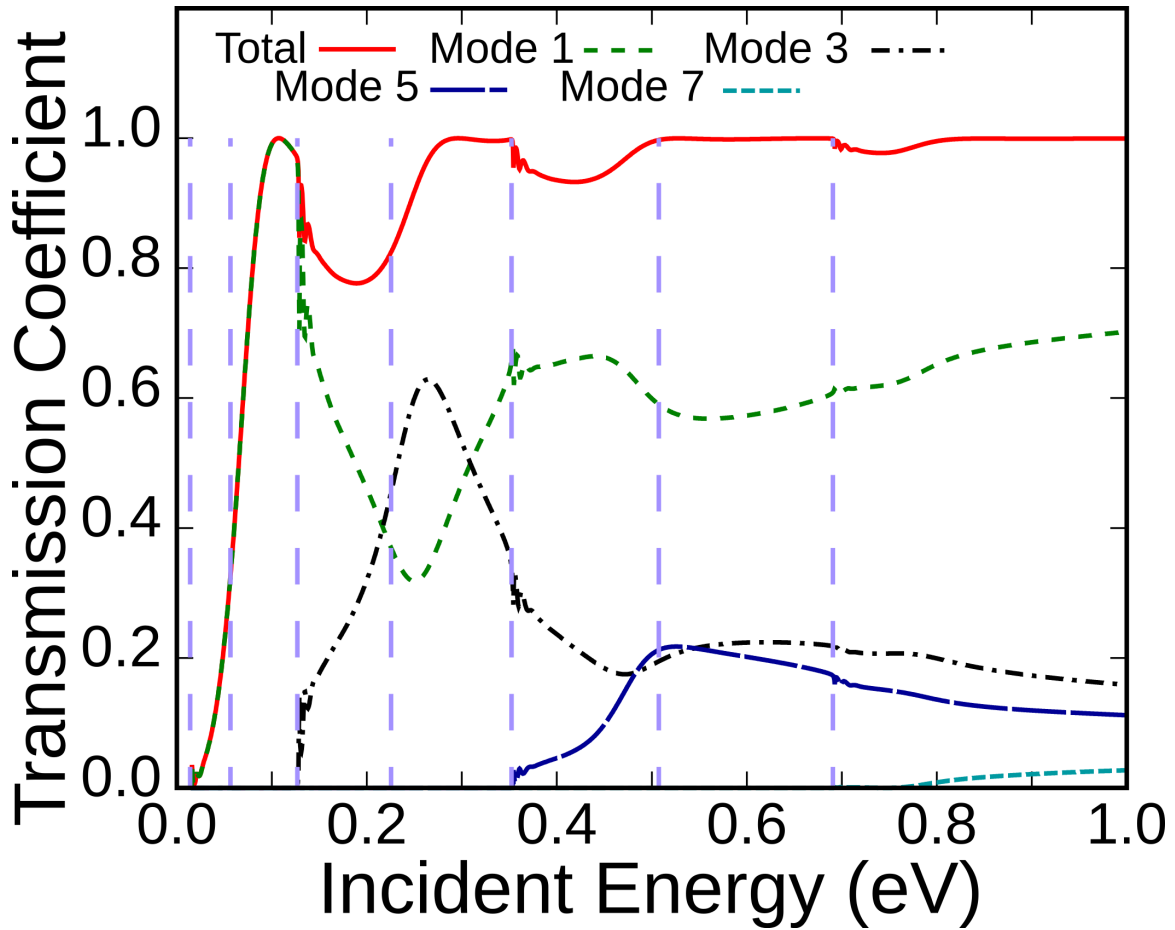


FIG. 23. The incident transmission versus energy plot for the lens scatterer, with no rotation, with an incident plane wave in mode $n=1$ is shown. Here we can see contribution from only odd modes due to the symmetry of the incident mode being preserved by the bilaterally symmetric square scatterer in the waveguide. The thresholds for each transmitted mode correspond to new a channel being opened. These thresholds are indicated by the vertical dashed lines.

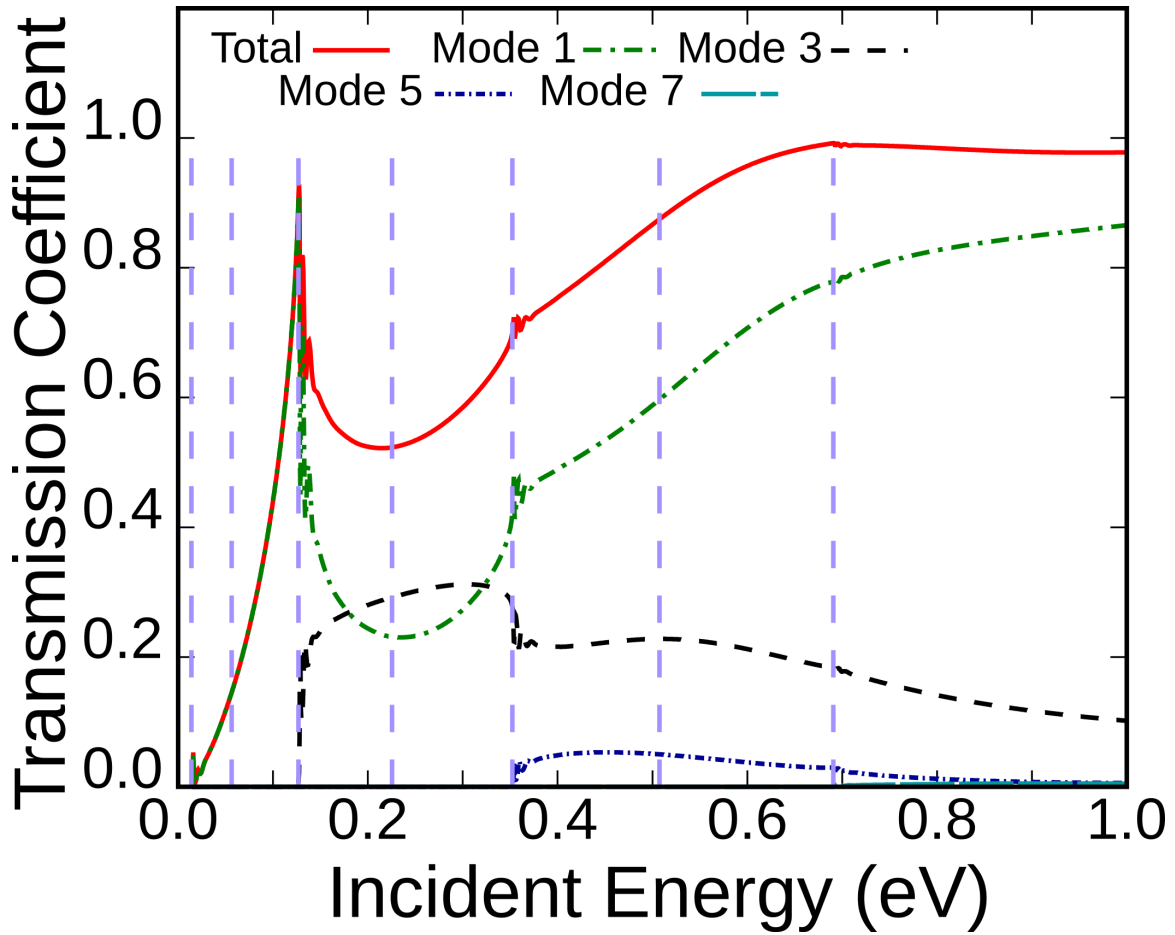


FIG. 24. The incident transmission versus energy plot for the lens scatterer, rotated 90 degrees, with an incident plane wave in mode $n=1$ is shown. Here we can see contribution from only odd modes due to the symmetry of the incident mode being preserved by the bilaterally symmetric square scatterer in the waveguide. The thresholds for each transmitted mode correspond to new a channel being opened. These thresholds are indicated by the vertical dashed lines.

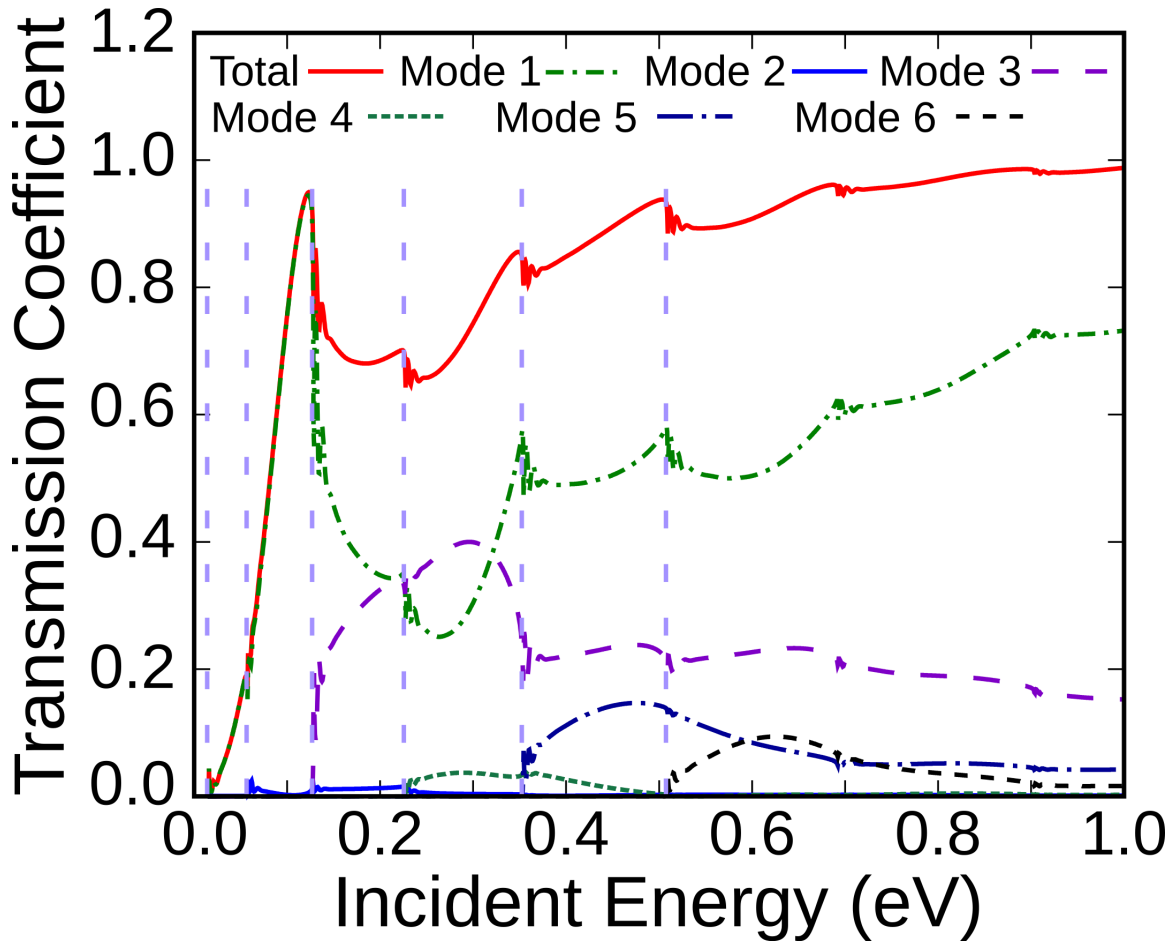


FIG. 25. The incident transmission versus energy plot for the lens scatterer, rotated 45 degrees, with an incident plane wave in mode $n=1$ is shown. Here we can see contribution from only odd modes due to the symmetry of the incident mode being preserved by the bilaterally symmetric square scatterer in the waveguide. The thresholds for each transmitted mode correspond to new a channel being opened. These thresholds are indicated by the vertical dashed lines.

G. Arbitrary scattering center: circular diffraction grating

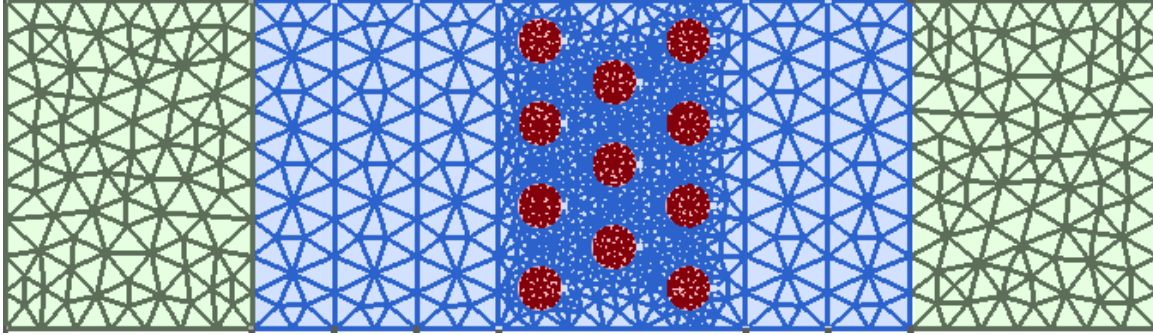


FIG. 26. The mesh used for the FEM calculation of the circular diffraction grating in a waveguide. The scattering centers are in red, the stealth region is in grey, and the propagation region is in blue.

In order to obtain an analytical solution for the geometry presented in Fig. 26 asymptotic boundary conditions, perturbation theory, and the First Born Approximation are used to obtain a solution. Even in the cases where a solution is obtainable, it rarely is ever in closed form. The finite element method allows for such a geometry to be modeled. Here we will show the results for incident modes up to $N=3$ for each arrangement of scattering centers, one row, two rows, and three rows of scatterers as shown in Fig. 26.

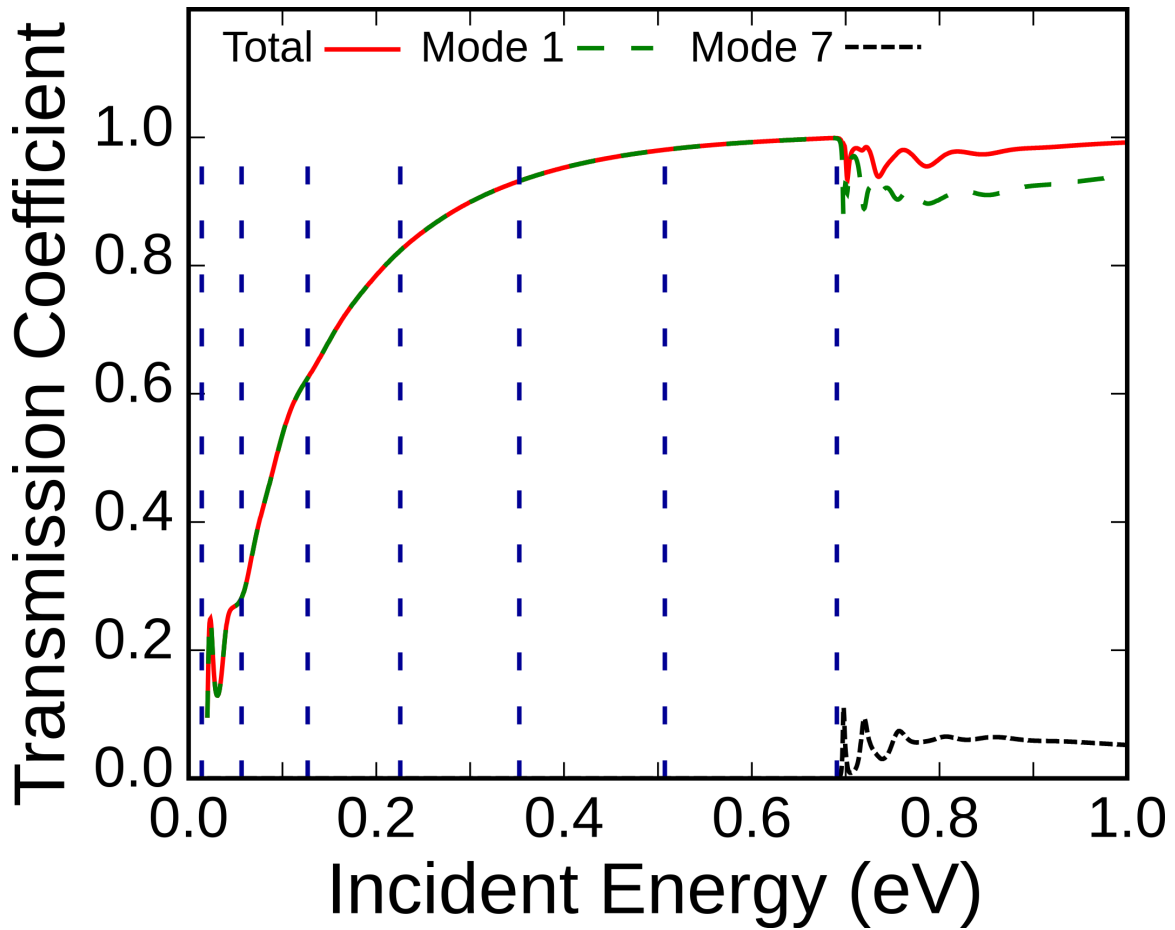


FIG. 27. The Incident Energy versus Transmission plot one row of circle scatterers, with incident mode of $n=1$. Here we can see contribution from only the odd modes, due to the symmetry of the incident mode being preserved. The threshold is the point at which new channels are opened, it corresponds to the energy levels of the cross-quantized modes.

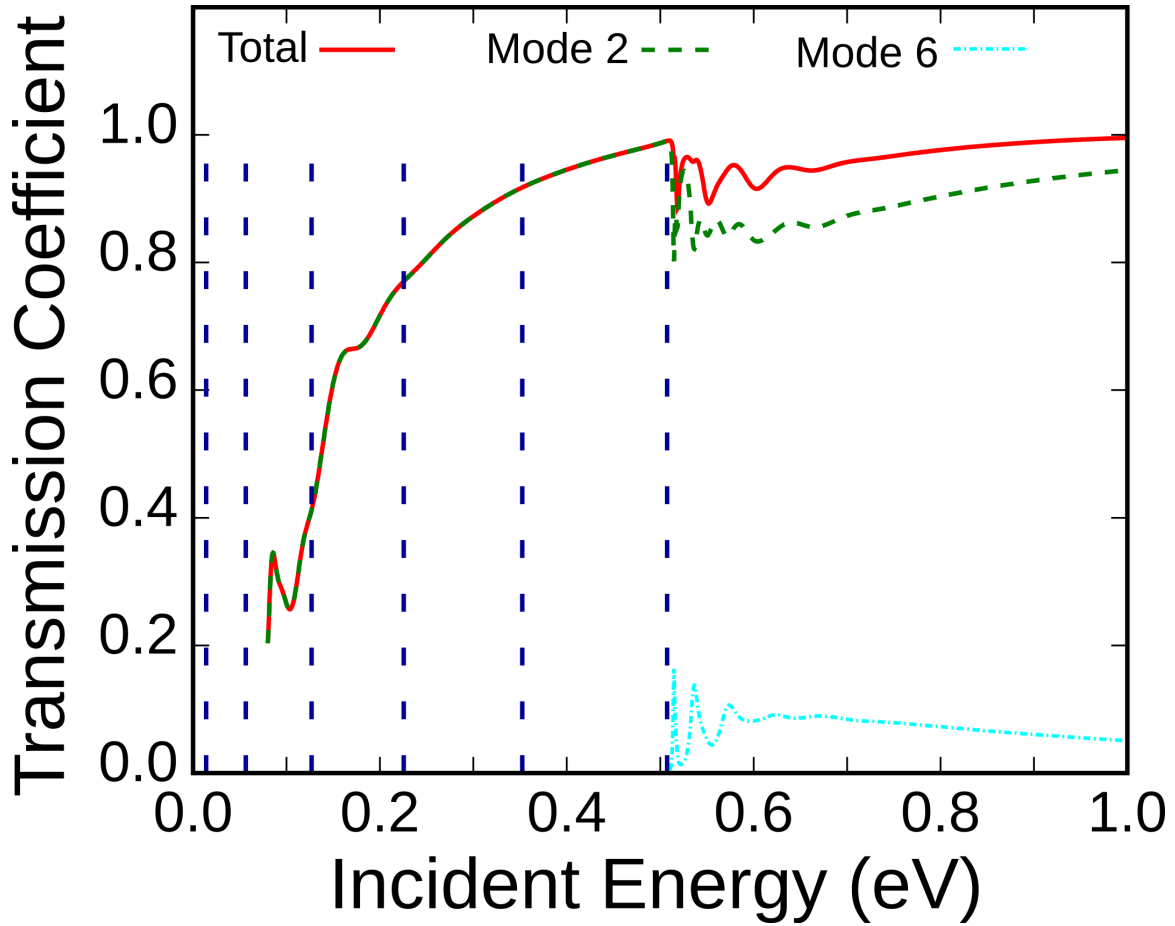


FIG. 28. The incident transmission versus energy plot for the diffraction grating with one row of scatterers, with an incident plane wave in mode $n=2$ is shown. Here we can see contribution from only even modes due to the symmetry of the incident mode being preserved by the bilaterally symmetric square scatterer in the waveguide. The thresholds for each transmitted mode correspond to new a channel being opened. These thresholds are indicated by the vertical dashed lines.

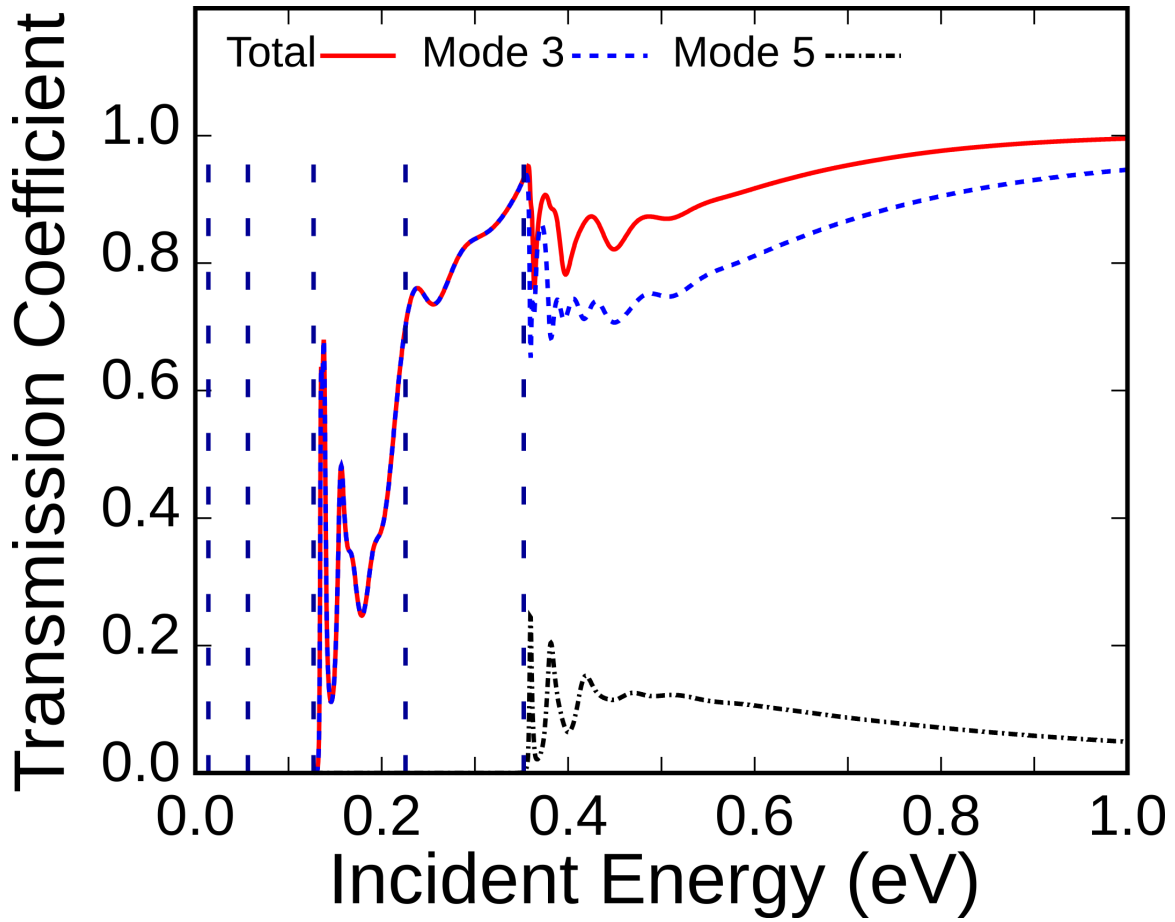


FIG. 29. The incident transmission versus energy plot for the diffraction grating with one row of scatterers, with an incident plane wave in mode $n=3$ is shown. Here we can see contribution from only odd modes due to the symmetry of the incident mode being preserved by the bilaterally symmetric square scatterer in the waveguide. The thresholds for each transmitted mode correspond to new a channel being opened. These thresholds are indicated by the vertical dashed lines.

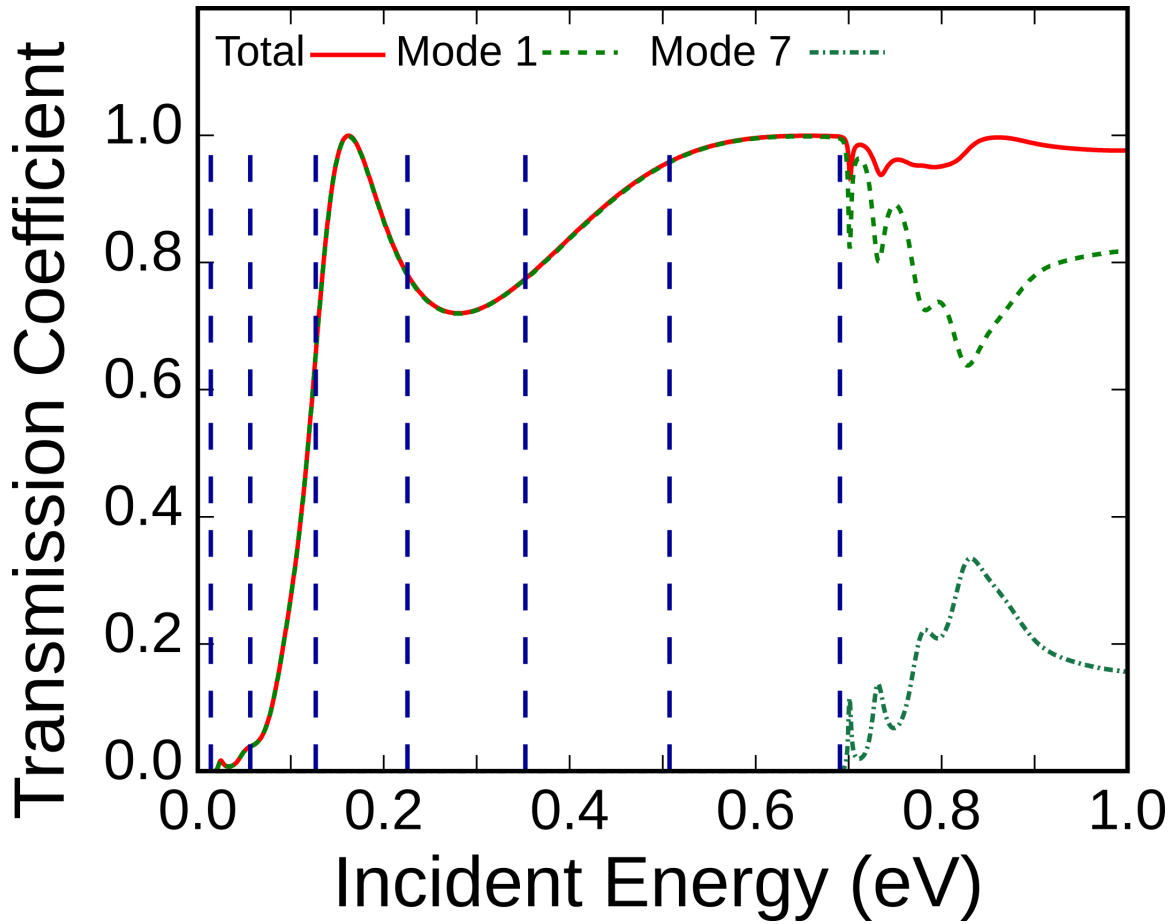


FIG. 30. The incident transmission versus energy plot for the diffraction grating with two rows of scatterers, with an incident plane wave in mode $n=1$ is shown. Here we can see contribution from only odd modes due to the symmetry of the incident mode being preserved by the bilaterally symmetric square scatterer in the waveguide. The thresholds for each transmitted mode correspond to new a channel being opened. These thresholds are indicated by the vertical dashed lines.

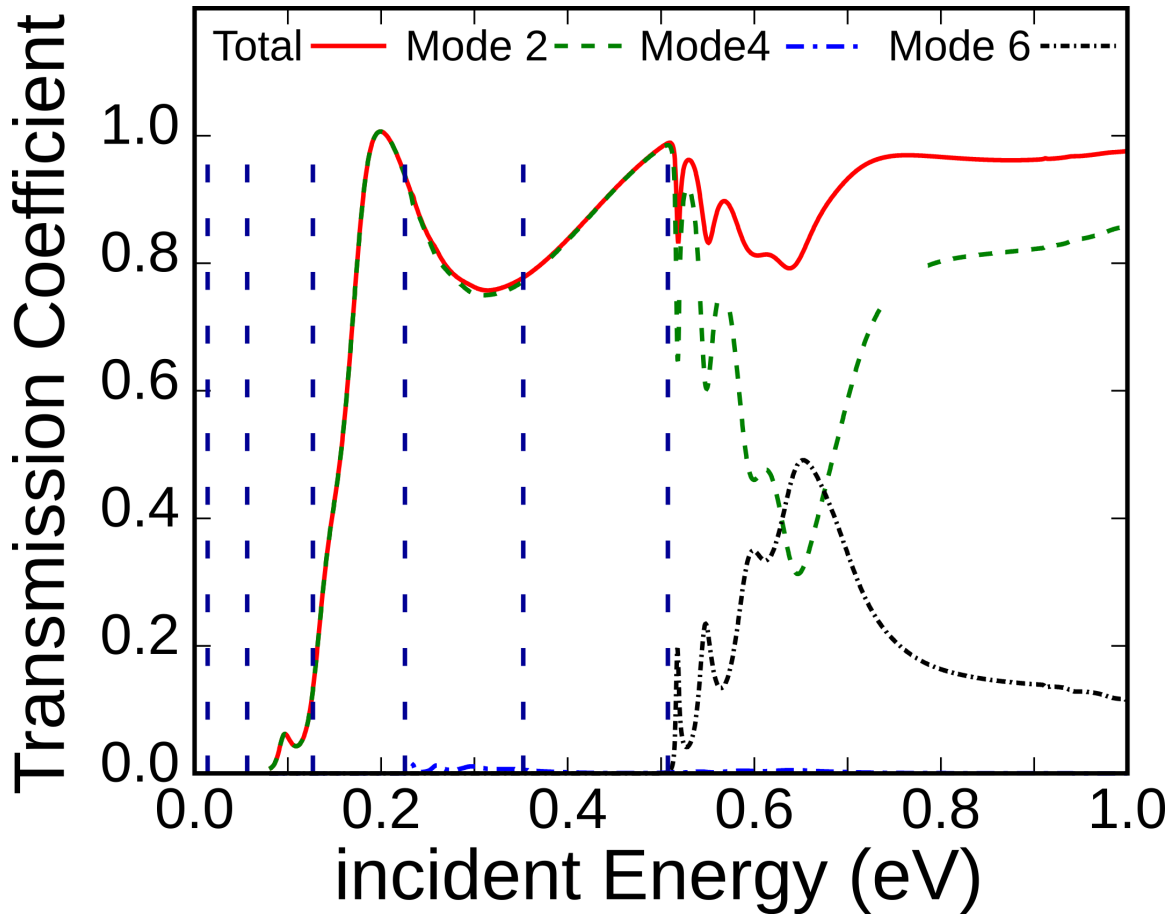


FIG. 31. The incident transmission versus energy plot for the diffraction grating with two rows of scatterers, with an incident plane wave in mode $n=2$ is shown. Here we can see contribution from only even modes due to the symmetry of the incident mode being preserved by the bilaterally symmetric square scatterer in the waveguide. The thresholds for each transmitted mode correspond to new a channel being opened. These thresholds are indicated by the vertical dashed lines.

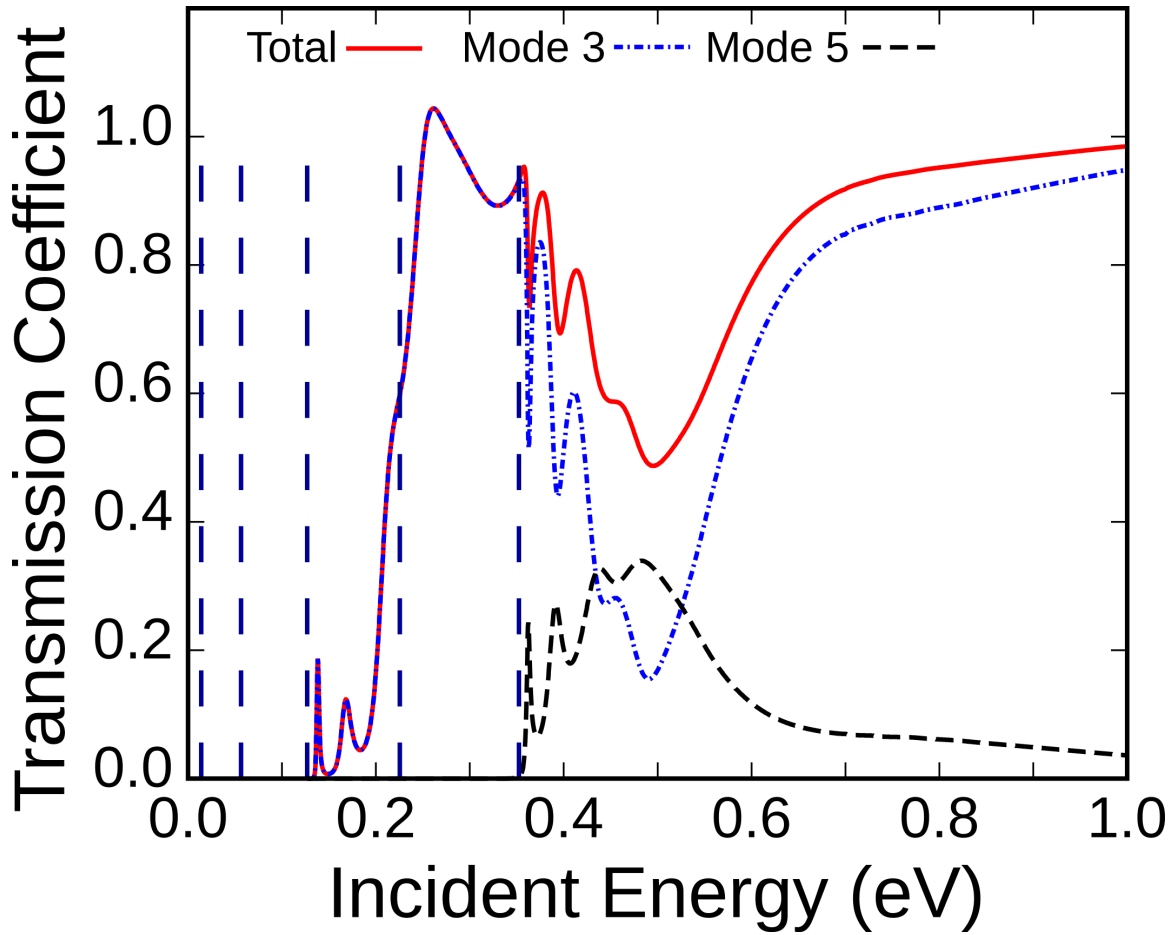


FIG. 32. The incident transmission versus energy plot for the diffraction grating with two rows of scatterers, with an incident plane wave in mode $n=3$ is shown. Here we can see contribution from only odd modes due to the symmetry of the incident mode being preserved by the bilaterally symmetric square scatterer in the waveguide. The thresholds for each transmitted mode correspond to new a channel being opened. These thresholds are indicated by the vertical dashed lines.

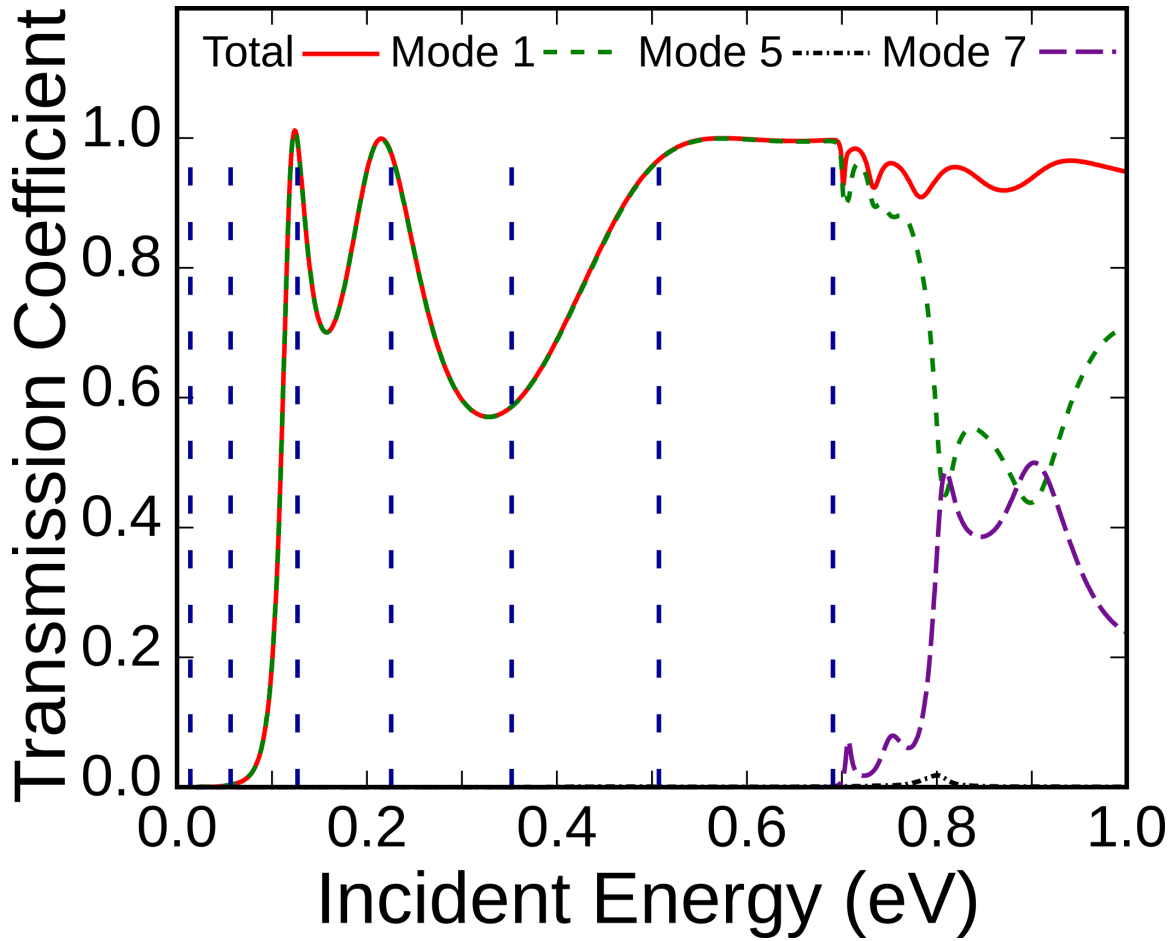


FIG. 33. The incident transmission versus energy plot for the diffraction grating with three rows of scatterers, with an incident plane wave in mode $n=1$ is shown. Here we can see contribution from only odd modes due to the symmetry of the incident mode being preserved by the bilaterally symmetric square scatterer in the waveguide. The thresholds for each transmitted mode correspond to new a channel being opened. These thresholds are indicated by the vertical dashed lines.

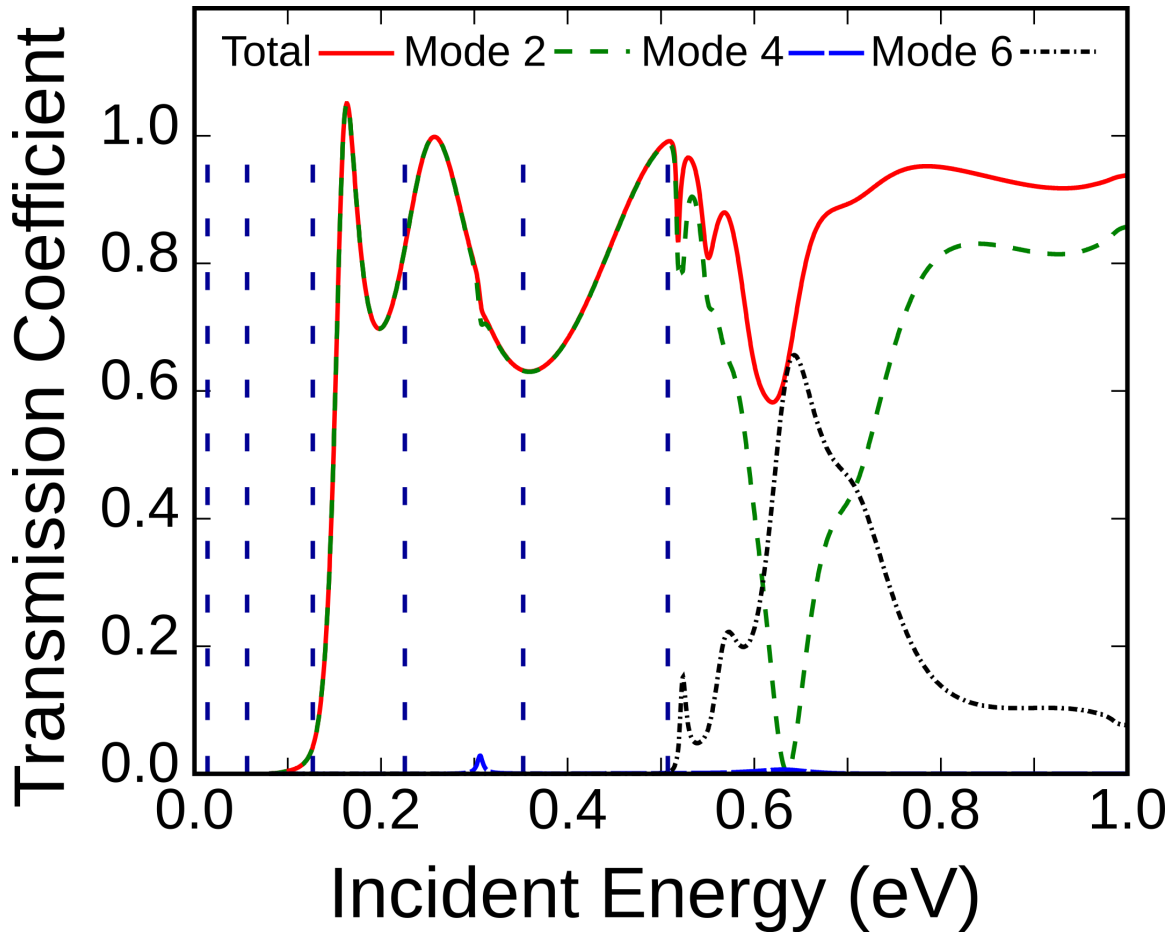


FIG. 34. The incident transmission versus energy plot for the diffraction grating with three rows of scatterers, with an incident plane wave in mode $n=2$ is shown. Here we can see contribution from only even modes due to the symmetry of the incident mode being preserved by the bilaterally symmetric square scatterer in the waveguide. The thresholds for each transmitted mode correspond to new a channel being opened. These thresholds are indicated by the vertical dashed lines.

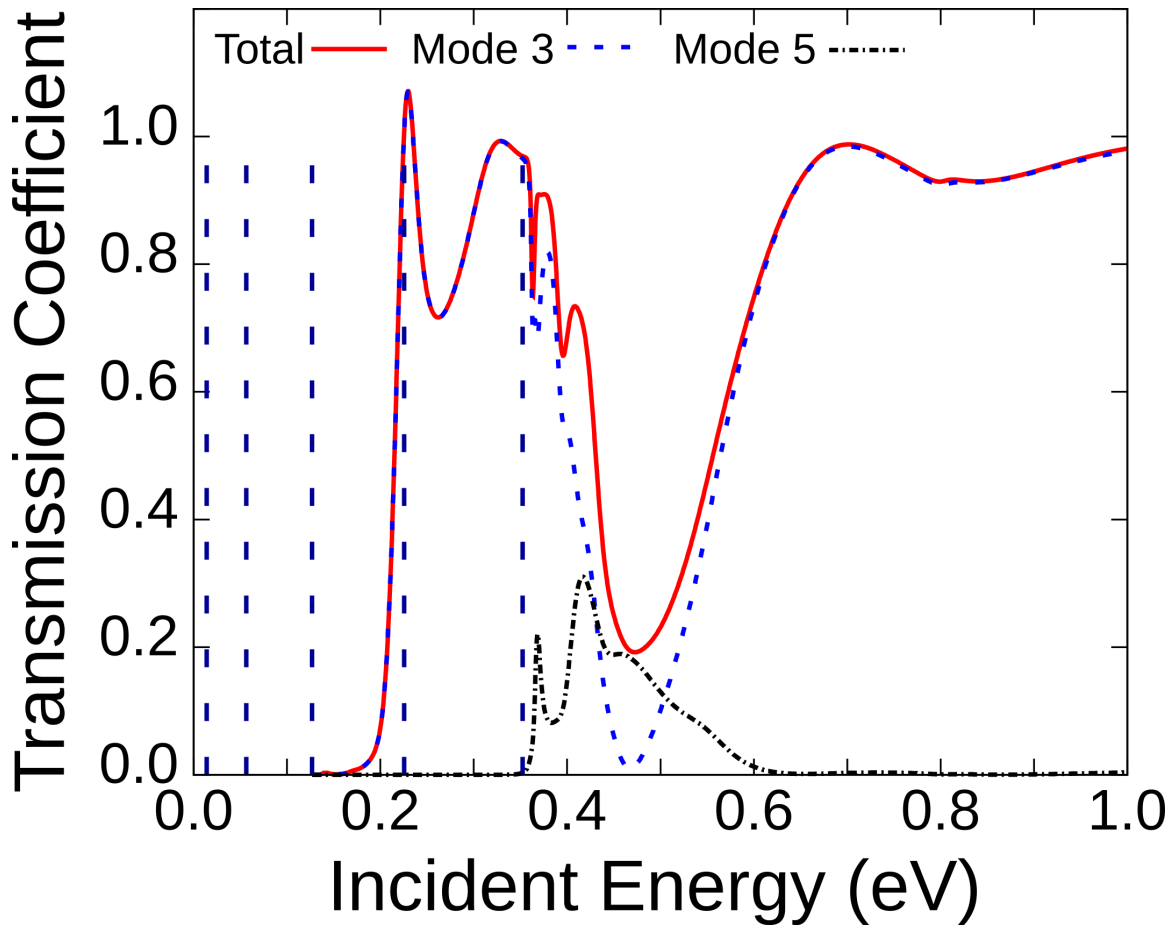


FIG. 35. The incident transmission versus energy plot for the diffraction grating with three rows of scatterers, with an incident plane wave in mode $n=3$ is shown. Here we can see contribution from only odd modes due to the symmetry of the incident mode being preserved by the bilaterally symmetric square scatterer in the waveguide. The thresholds for each transmitted mode correspond to new a channel being opened. These thresholds are indicated by the vertical dashed lines.

H. Curved waveguides

The finite element method allows arbitrary geometries to be computed easily. This makes FEM a good technique for doing computations on curved waveguides. The results for a waveguide with inner radius .1 angstroms, outer radius 100.1 angstroms with a 180 degree bend are given below.

1. Boundary conditions

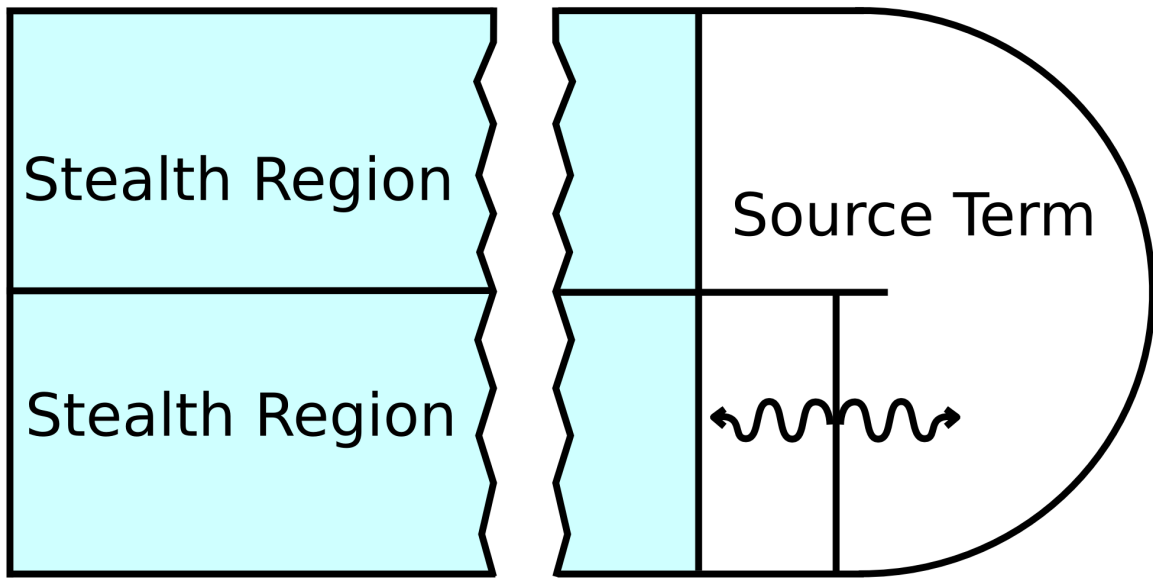


FIG. 36. The Geometry of the curved waveguide, showing the stealth region and source.

Fig. 36 shows the geometry being used. Stealth elements are placed on the left to simplify the BCs in that region. On the curved section, the BCs require the wavefunction and its derivatives along the boundary to vanish. This is accomplished by approximating the tangent of the curve by the line connecting a boundary node to its nearest neighboring boundary node. Once this tangent line is obtained, we must ensure that the function, and its derivatives, perpendicular to it, are set to zero.

2. Results

Goldstone and others^{12,13,15-18} have shown that there exists a bound state in such a waveguide. In fact it has been determined that there will be a bound state in any curved

waveguide,¹² however, we found that for certain curve radii, the resonant states do not reach full resonance, which would correspond to a reflection coefficient of 100%. When considering device design, these radial lengths would be an ineffective choice if a total reflection is desired.

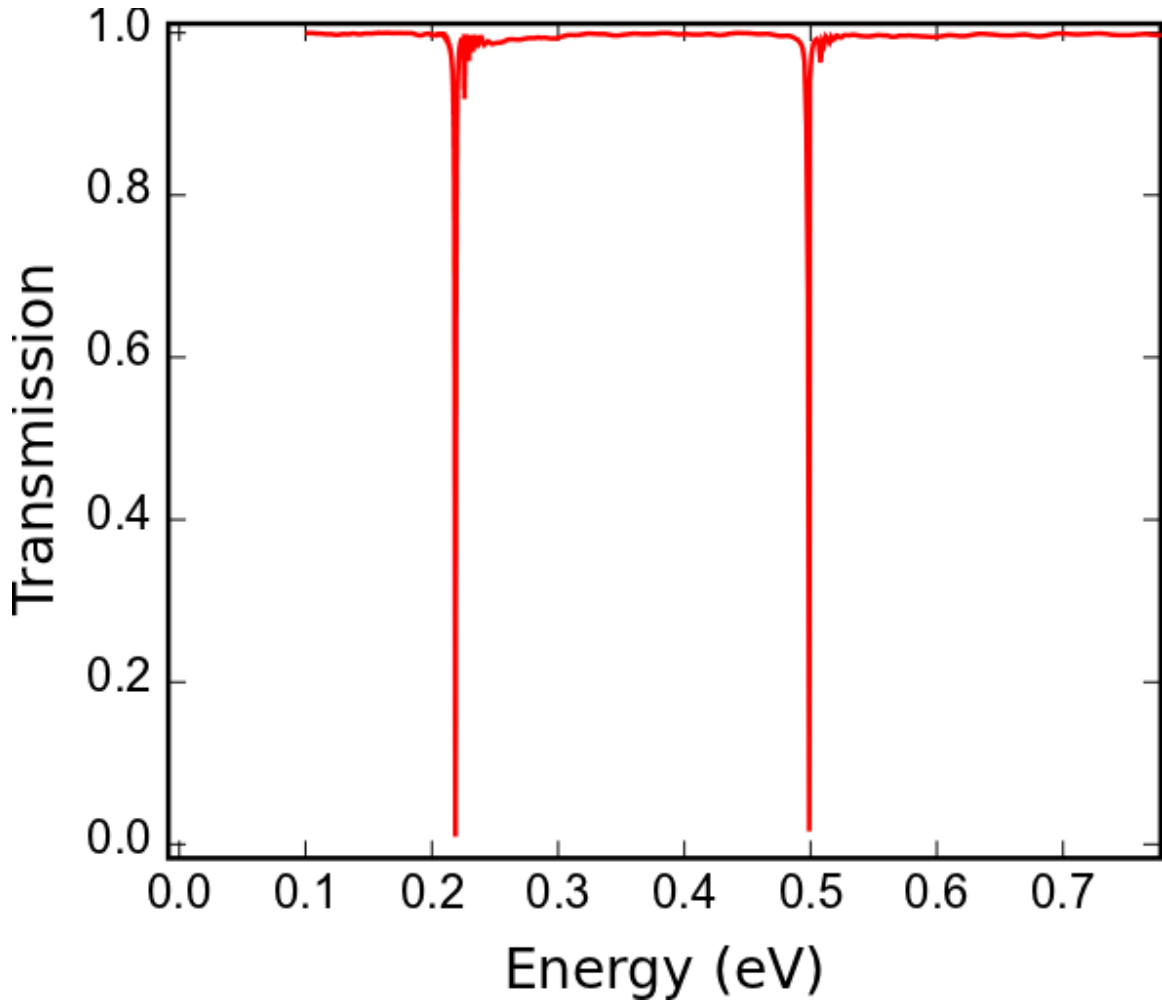


FIG. 37. The transmission coefficient as a function of incident energy for the curved waveguide is shown.

Fig. 37 shows a plot of transmission versus energy through the bent waveguide. This data was collected by running an FEM simulation for each energy sampled and calculating the reflection and transmission using the calculated wavefunction. As expected, several resonant states corresponding to the bound states are shown. The probability current of the ground state wave function is shown in Fig. 38. In this instance the dips in transmission can be thought of as *anti-resonances*.

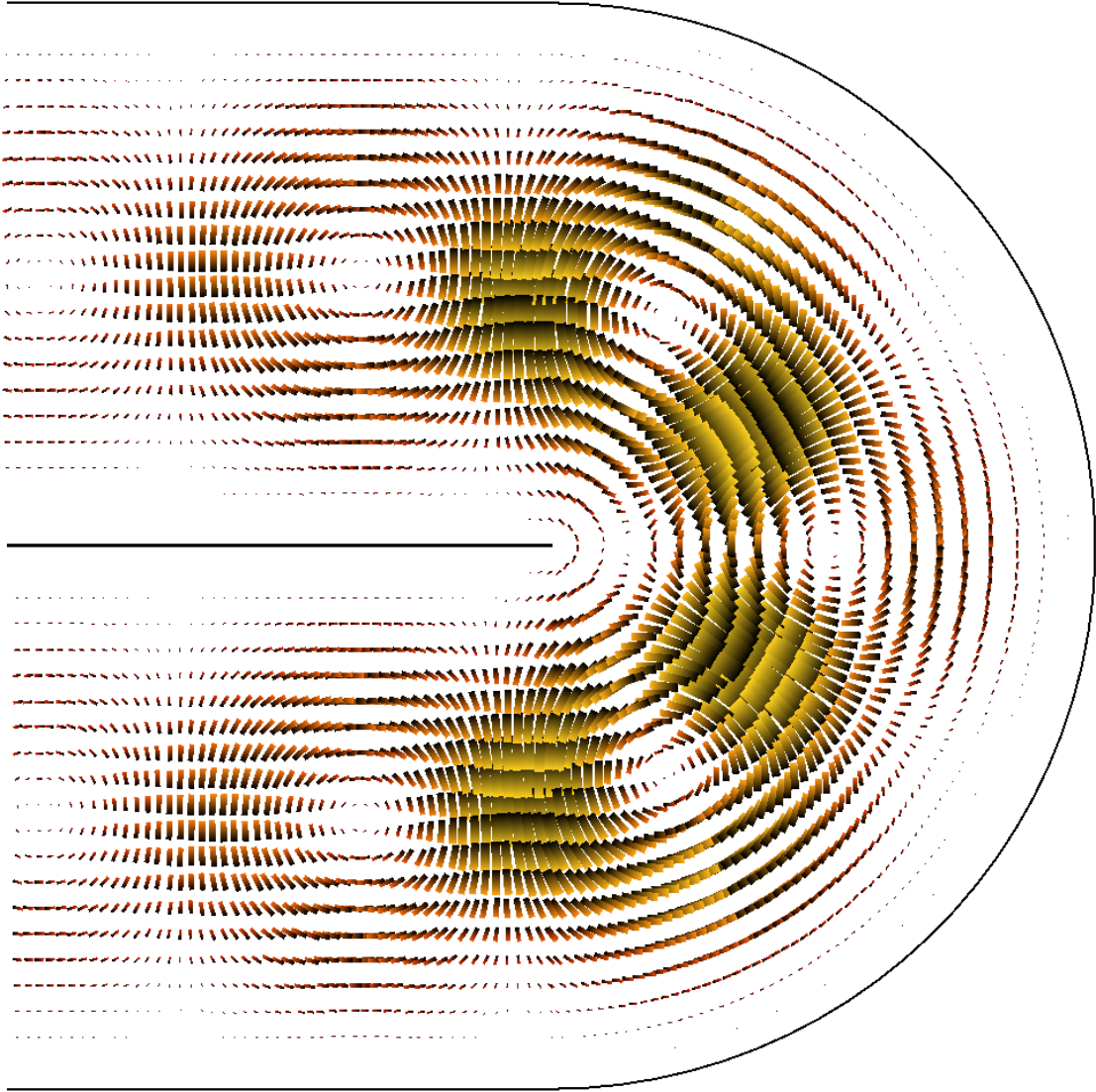


FIG. 38. The probability current for the first resonant state in the curved waveguide is shown. Note the localization of the waveguide due to the bend, leading to total reflection.

I. Additional Results

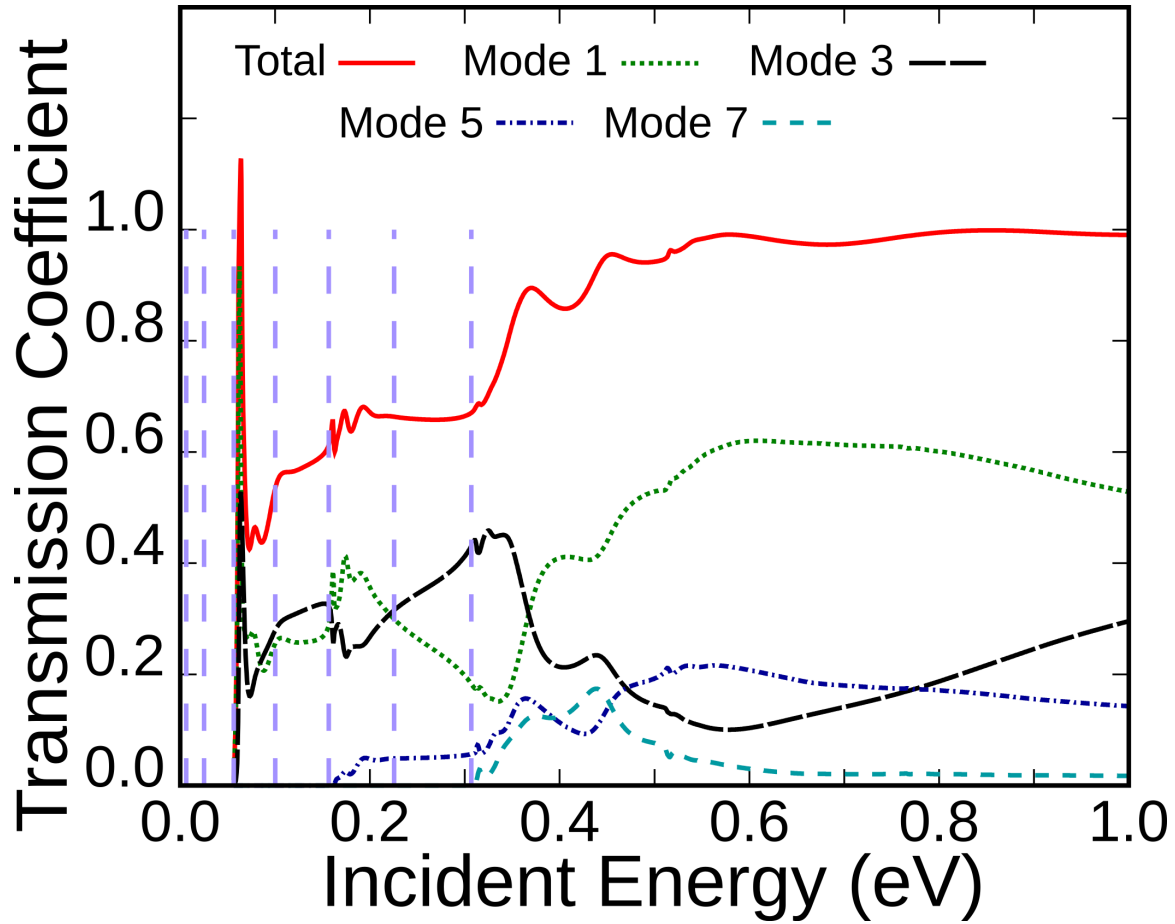


FIG. 39. The incident transmission versus energy plot for the square scatterer, with an incident plane wave in mode $n=3$ is shown. Here we can see contribution from only odd modes due to the symmetry of the incident mode being preserved by the bilaterally symmetric square scatterer in the waveguide. The thresholds for each transmitted mode correspond to new a channel being opened. These thresholds are indicated by the vertical dashed lines.

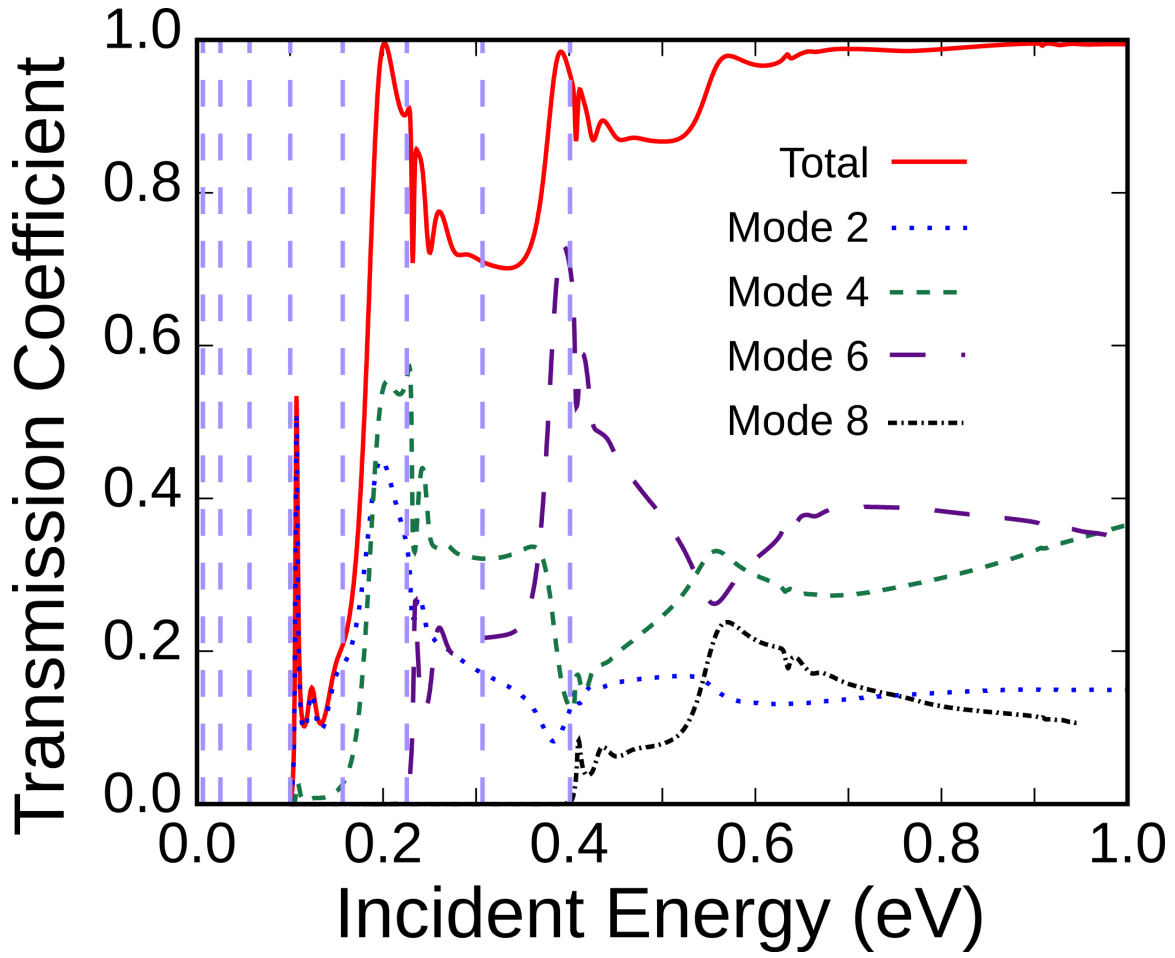


FIG. 40. The incident transmission versus energy plot for the square scatterer, with an incident plane wave in mode $n=4$ is shown. Here we can see contribution from only even modes due to the symmetry of the incident mode being preserved by the bilaterally symmetric square scatterer in the waveguide. The thresholds for each transmitted mode correspond to new a channel being opened. These thresholds are indicated by the vertical dashed lines.

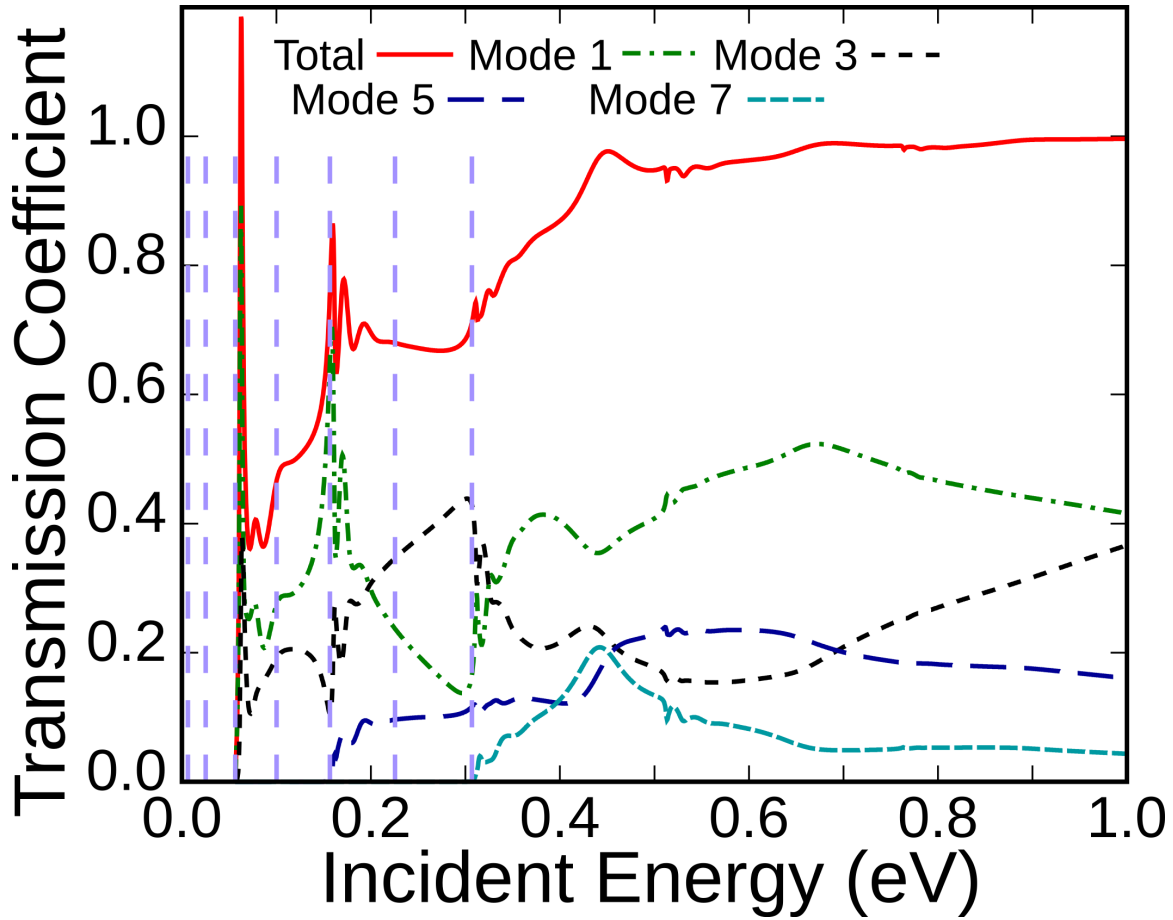


FIG. 41. The incident transmission versus energy plot for the circular scatterer, with an incident plane wave in mode $n=3$ is shown. Here we can see contribution from only odd modes due to the symmetry of the incident mode being preserved by the bilaterally symmetric square scatterer in the waveguide. The thresholds for each transmitted mode correspond to new a channel being opened. These thresholds are indicated by the vertical dashed lines.

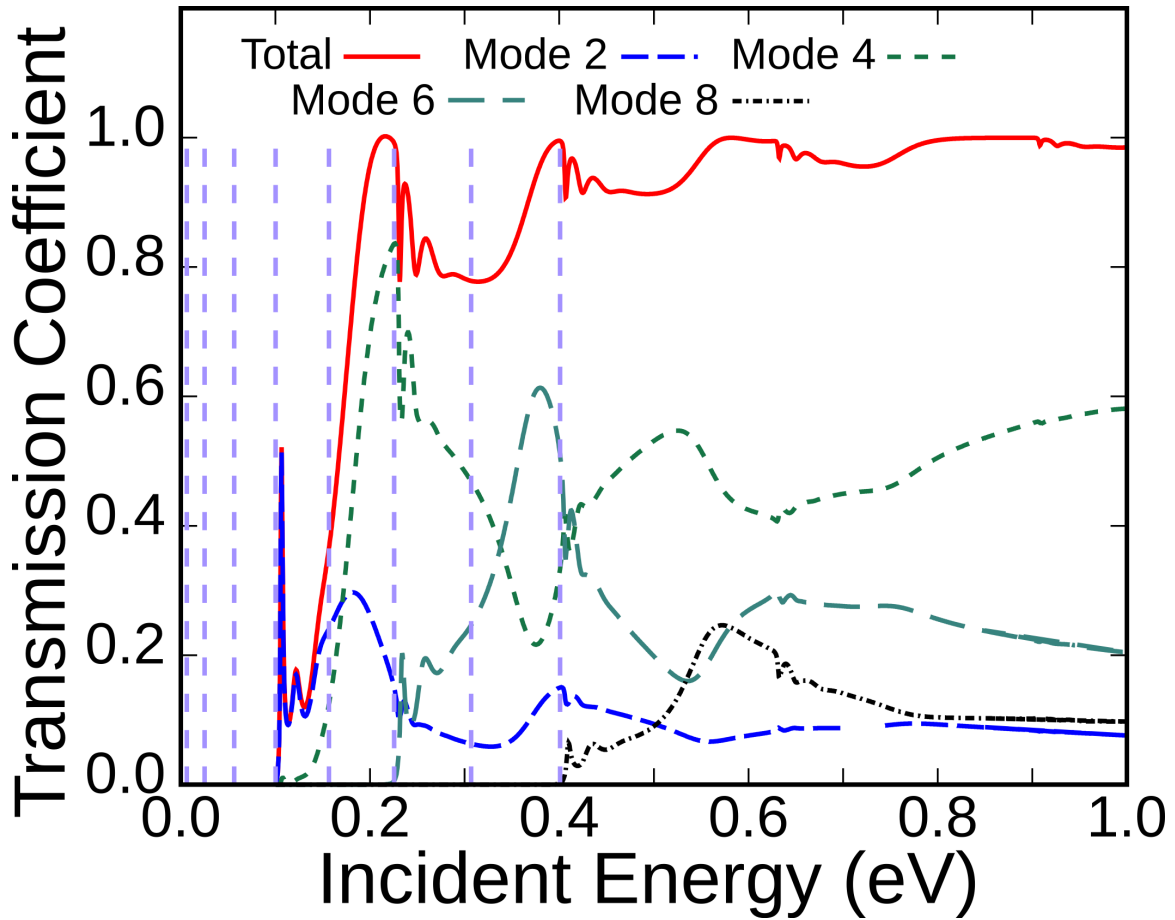


FIG. 42. The incident transmission versus energy plot for the circular scatterer, with an incident plane wave in mode $n=4$ is shown. Here we can see contribution from only even modes due to the symmetry of the incident mode being preserved by the bilaterally symmetric square scatterer in the waveguide. The thresholds for each transmitted mode correspond to new a channel being opened. These thresholds are indicated by the vertical dashed lines.

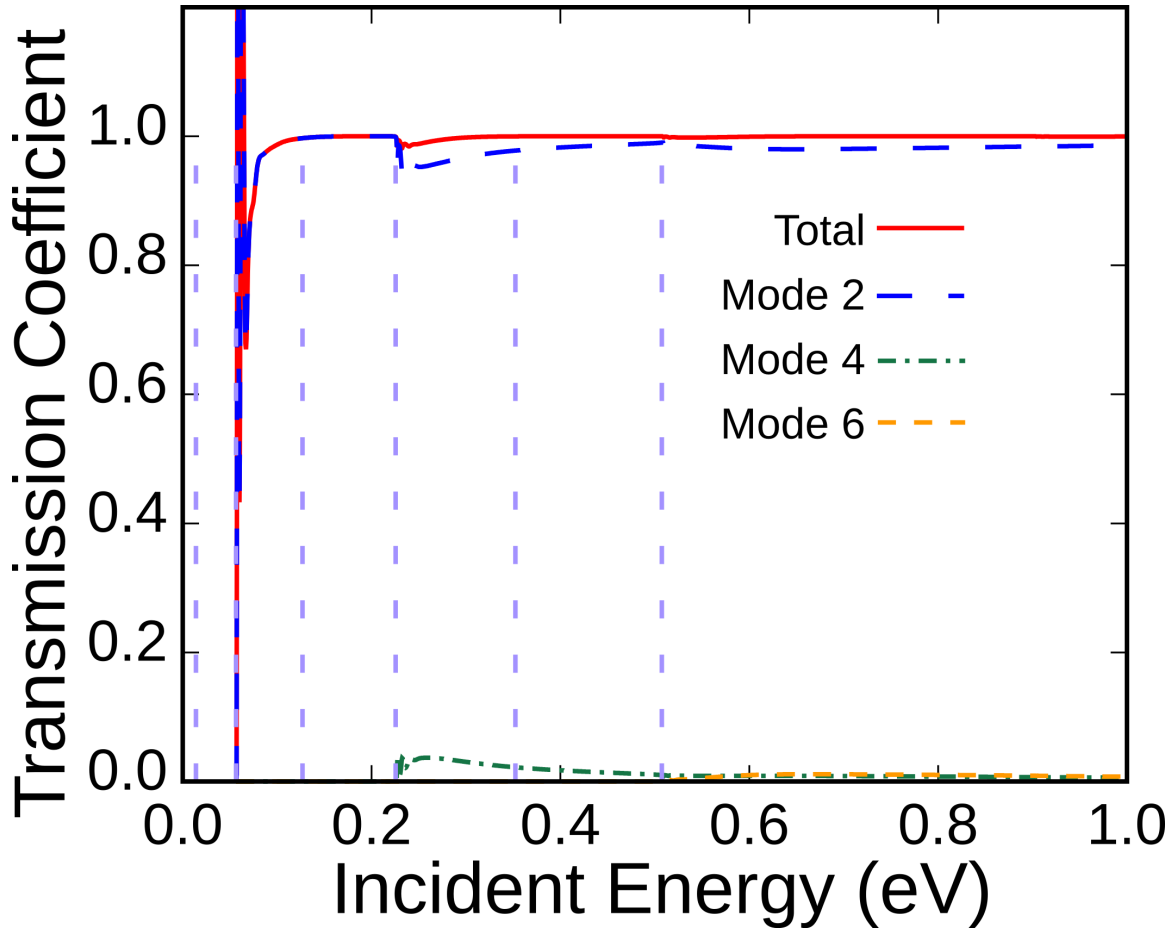


FIG. 43. The incident transmission versus energy plot for the lens scatterer, with no rotation, with an incident plane wave in mode $n=2$ is shown. Here we can see contribution from only even modes due to the symmetry of the incident mode being preserved by the bilaterally symmetric square scatterer in the waveguide. The thresholds for each transmitted mode correspond to new a channel being opened. These thresholds are indicated by the vertical dashed lines.

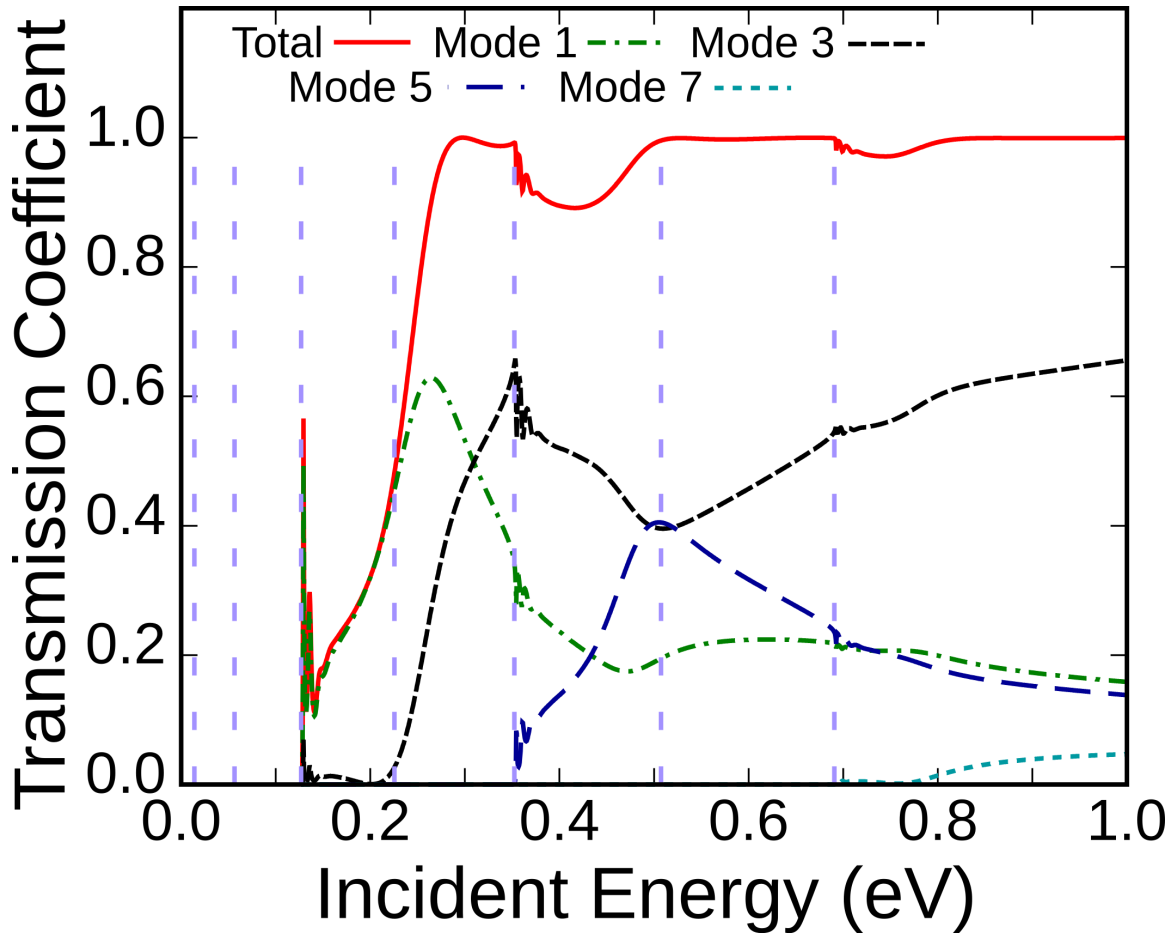


FIG. 44. The incident transmission versus energy plot for the lens scatterer, with no rotation, with an incident plane wave in mode $n=3$ is shown. Here we can see contribution from only odd modes due to the symmetry of the incident mode being preserved by the bilaterally symmetric square scatterer in the waveguide. The thresholds for each transmitted mode correspond to new a channel being opened. These thresholds are indicated by the vertical dashed lines.

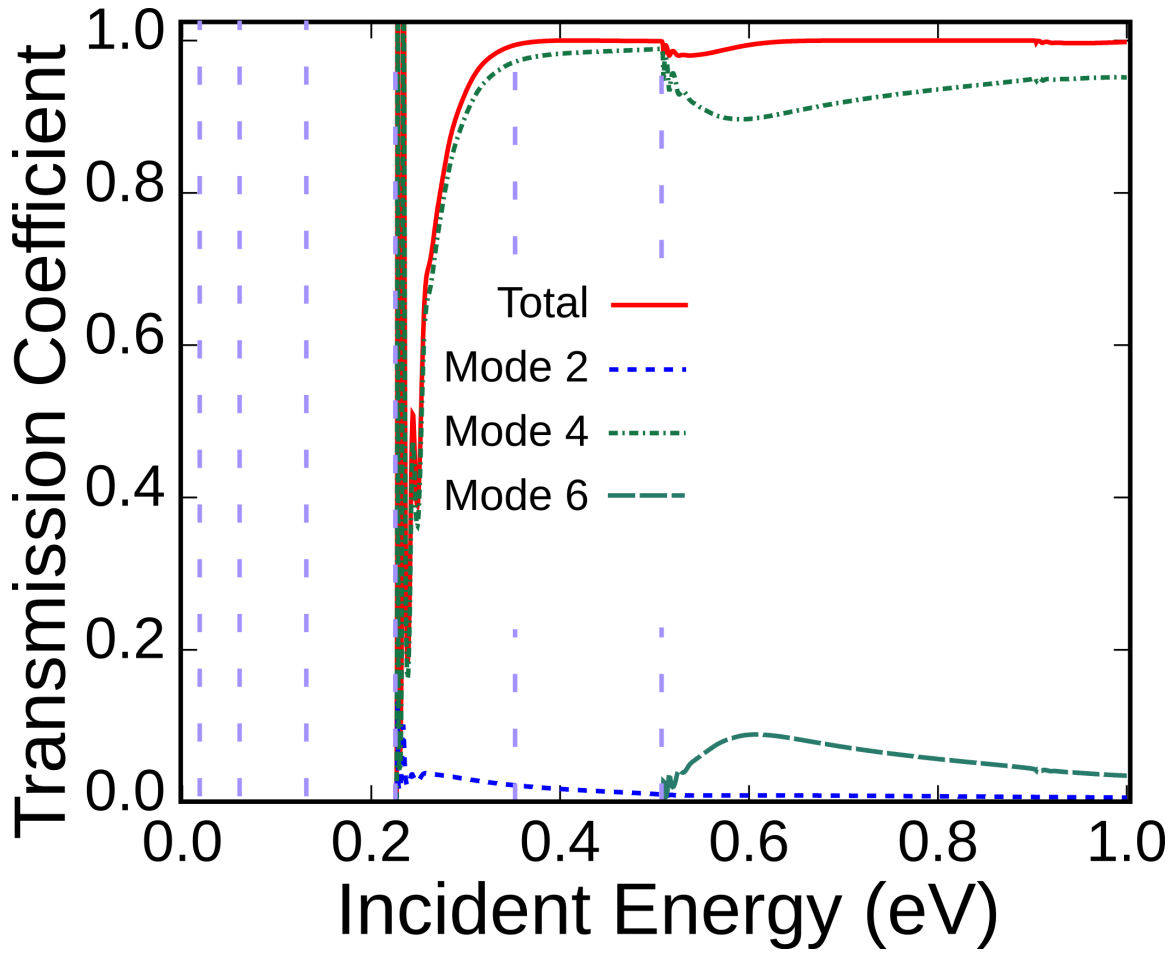


FIG. 45. The incident transmission versus energy plot for the lens scatterer, with no rotation, with an incident plane wave in mode $n=4$ is shown. Here we can see contribution from only even modes due to the symmetry of the incident mode being preserved by the bilaterally symmetric square scatterer in the waveguide. The thresholds for each transmitted mode correspond to new a channel being opened. These thresholds are indicated by the vertical dashed lines.

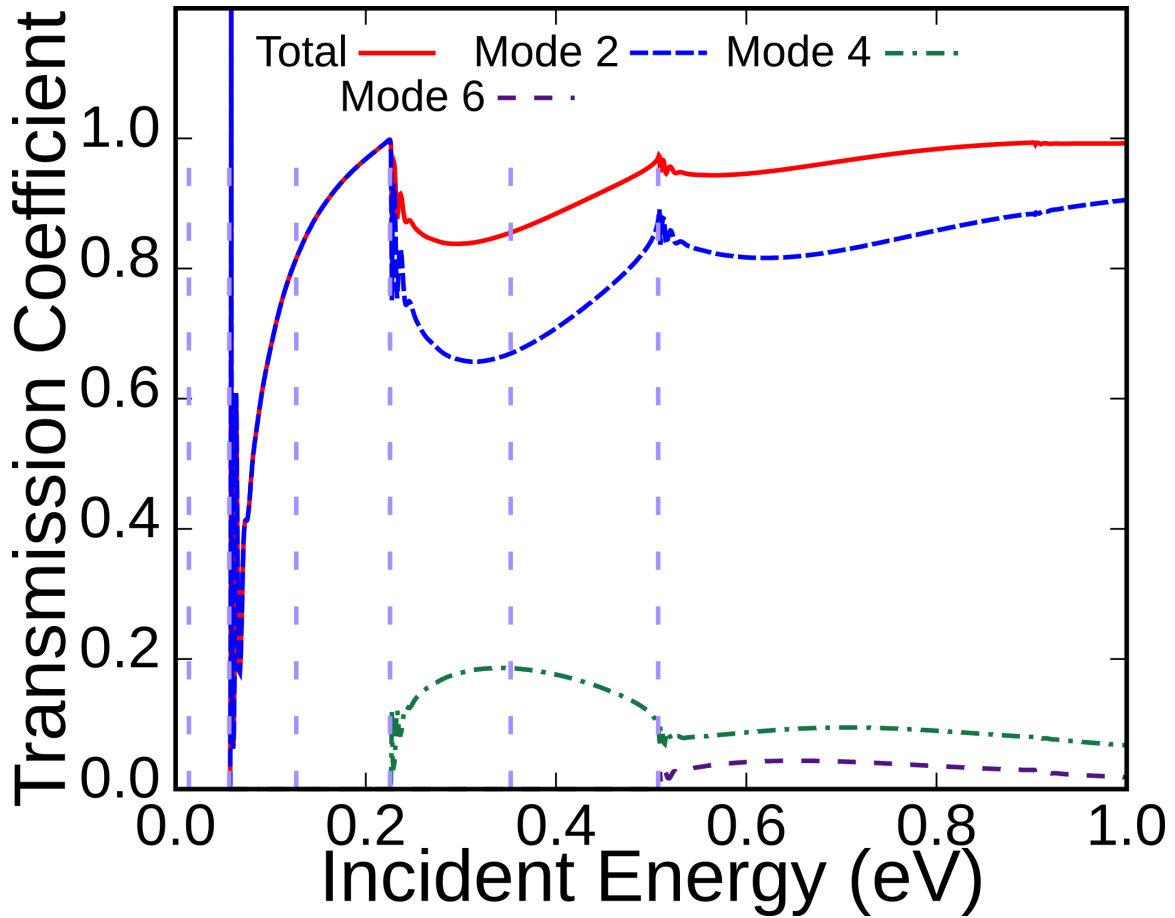


FIG. 46. The incident transmission versus energy plot for the lens scatterer, rotated 90 degrees, with an incident plane wave in mode $n=2$ is shown. Here we can see contribution from only even modes due to the symmetry of the incident mode being preserved by the bilaterally symmetric square scatterer in the waveguide. The thresholds for each transmitted mode correspond to new a channel being opened. These thresholds are indicated by the vertical dashed lines.

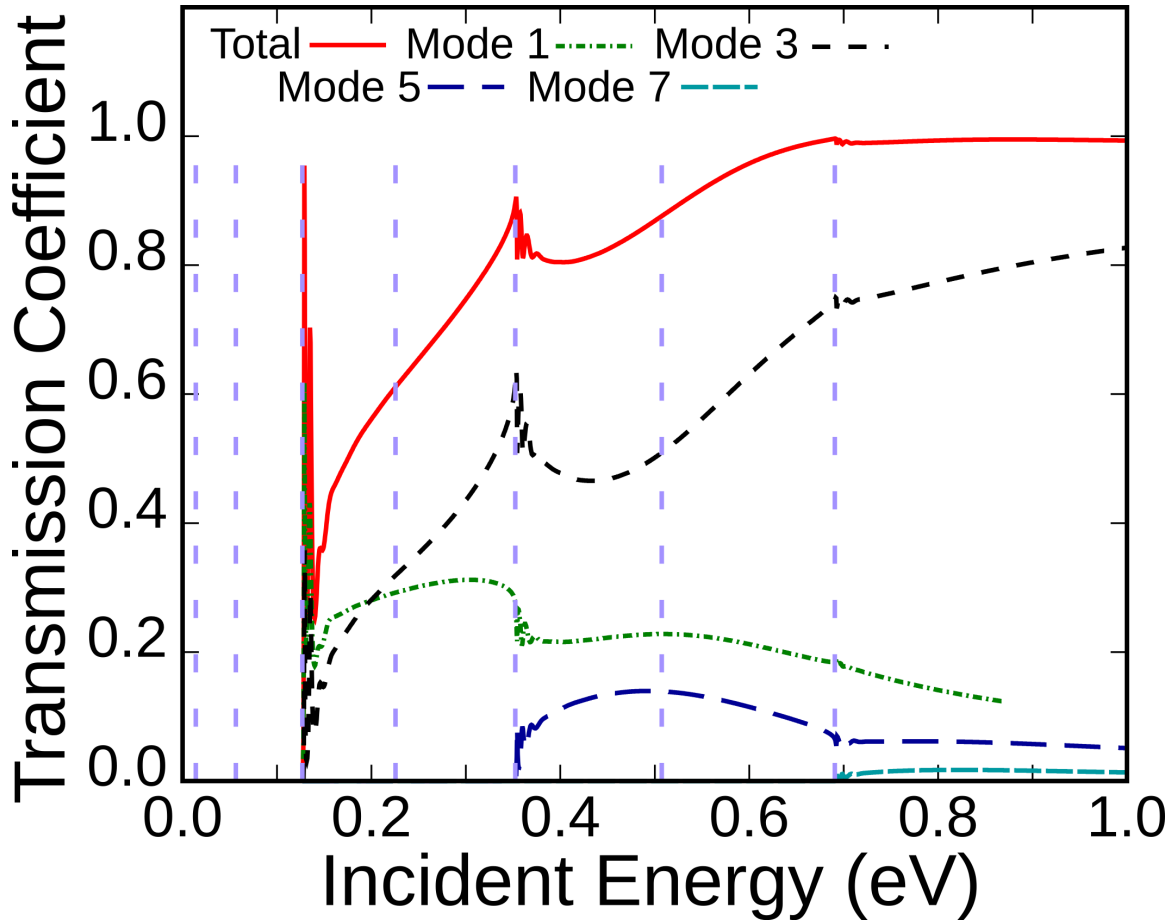


FIG. 47. The incident transmission versus energy plot for the lens scatterer, rotated 90 degrees, with an incident plane wave in mode $n=3$ is shown. Here we can see contribution from only odd modes due to the symmetry of the incident mode being preserved by the bilaterally symmetric square scatterer in the waveguide. The thresholds for each transmitted mode correspond to new a channel being opened. These thresholds are indicated by the vertical dashed lines.

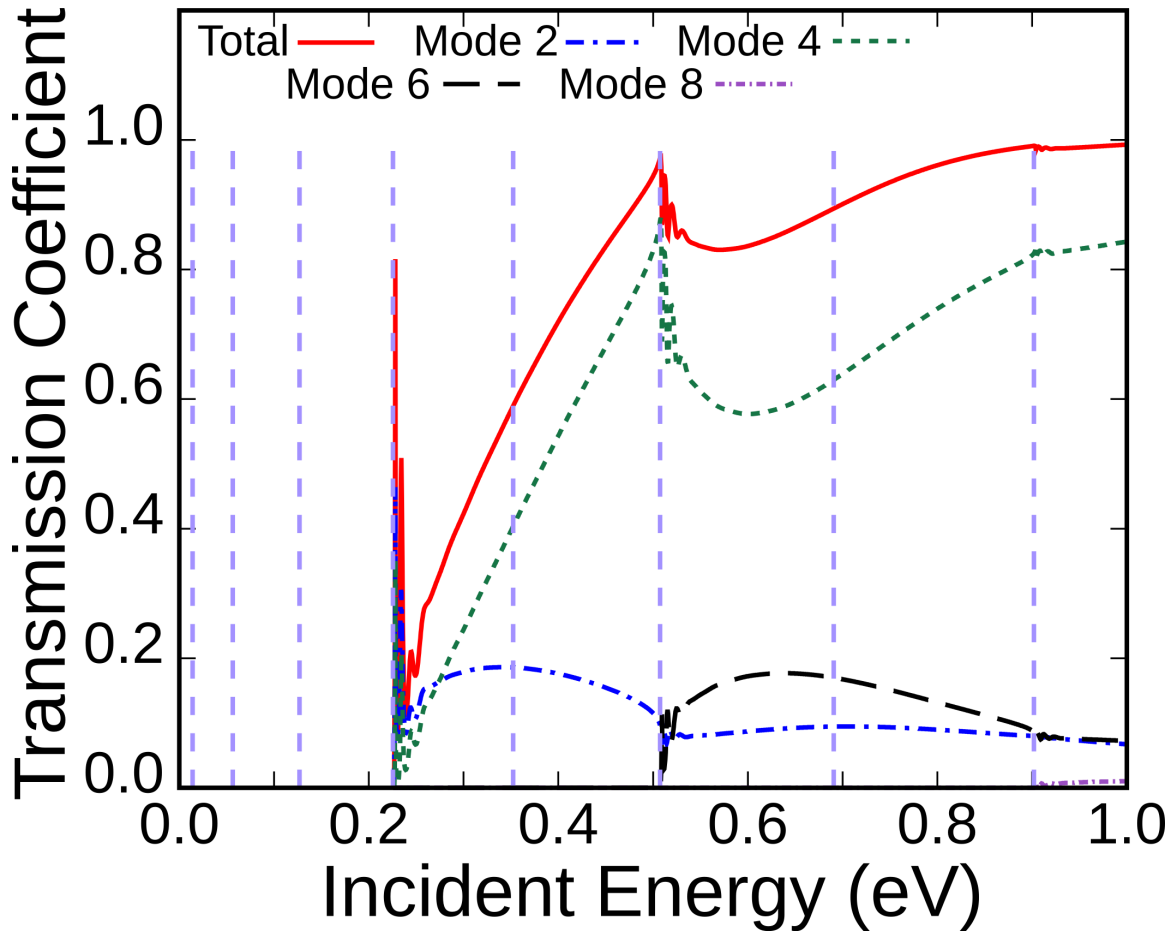


FIG. 48. The incident transmission versus energy plot for the lens scatterer, rotated 90 degrees, with an incident plane wave in mode $n=4$ is shown. Here we can see contribution from only even modes due to the symmetry of the incident mode being preserved by the bilaterally symmetric square scatterer in the waveguide. The thresholds for each transmitted mode correspond to new a channel being opened. These thresholds are indicated by the vertical dashed lines.

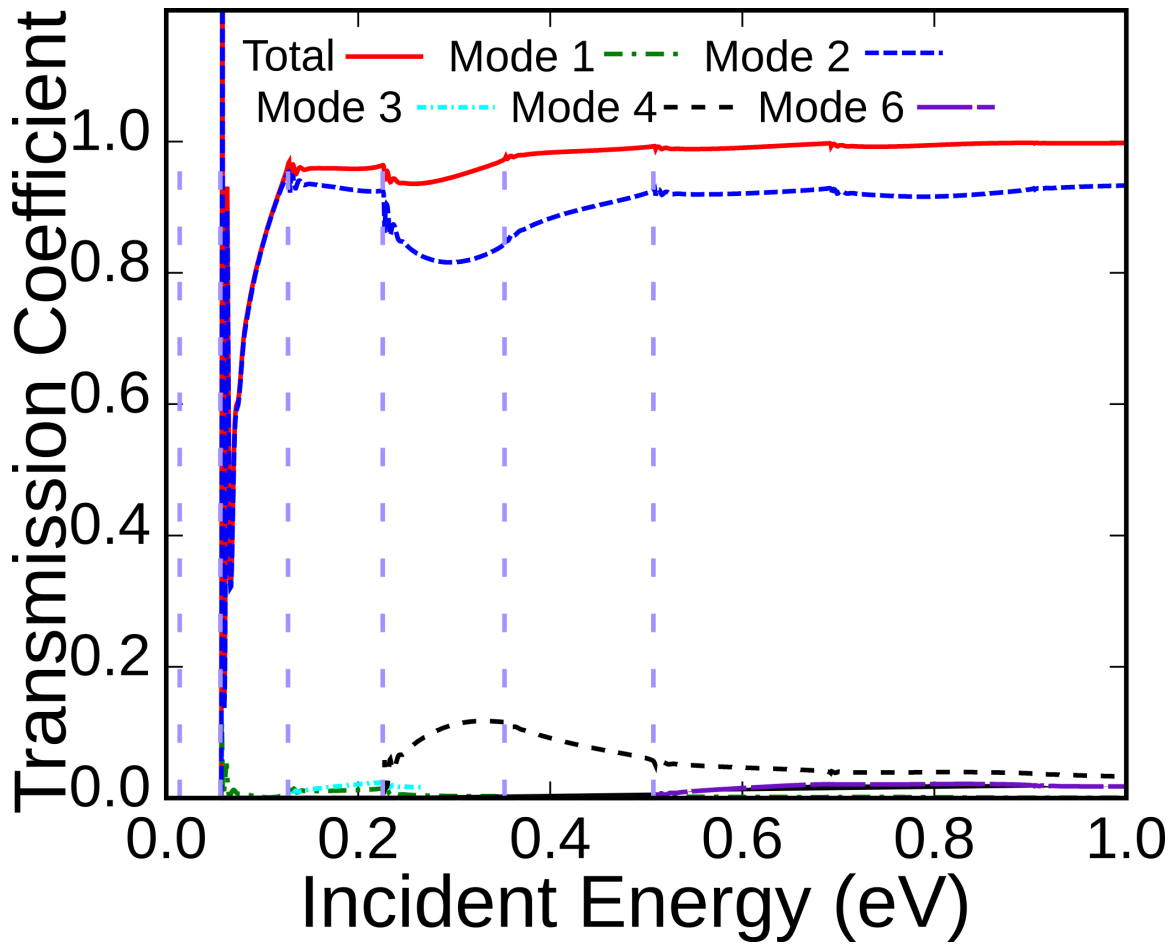


FIG. 49. The incident transmission versus energy plot for the lens scatterer, rotated 45 degrees, with an incident plane wave in mode $n=2$ is shown. Here we can see contribution from only even modes due to the symmetry of the incident mode being preserved by the bilaterally symmetric square scatterer in the waveguide. The thresholds for each transmitted mode correspond to new a channel being opened. These thresholds are indicated by the vertical dashed lines.

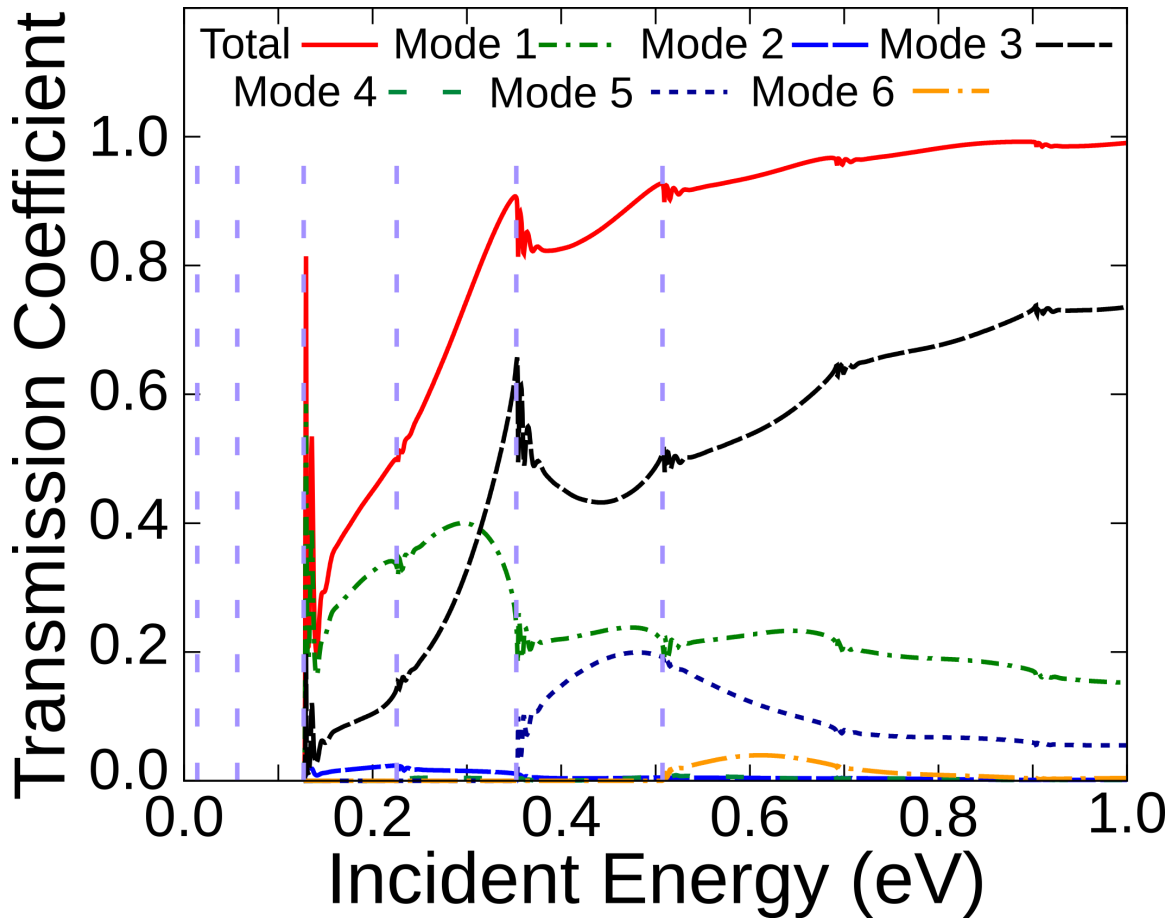


FIG. 50. The incident transmission versus energy plot for the lens scatterer, rotated 45 degrees, with an incident plane wave in mode $n=3$ is shown. Here we can see contribution from only odd modes due to the symmetry of the incident mode being preserved by the bilaterally symmetric square scatterer in the waveguide. The thresholds for each transmitted mode correspond to new a channel being opened. These thresholds are indicated by the vertical dashed lines.

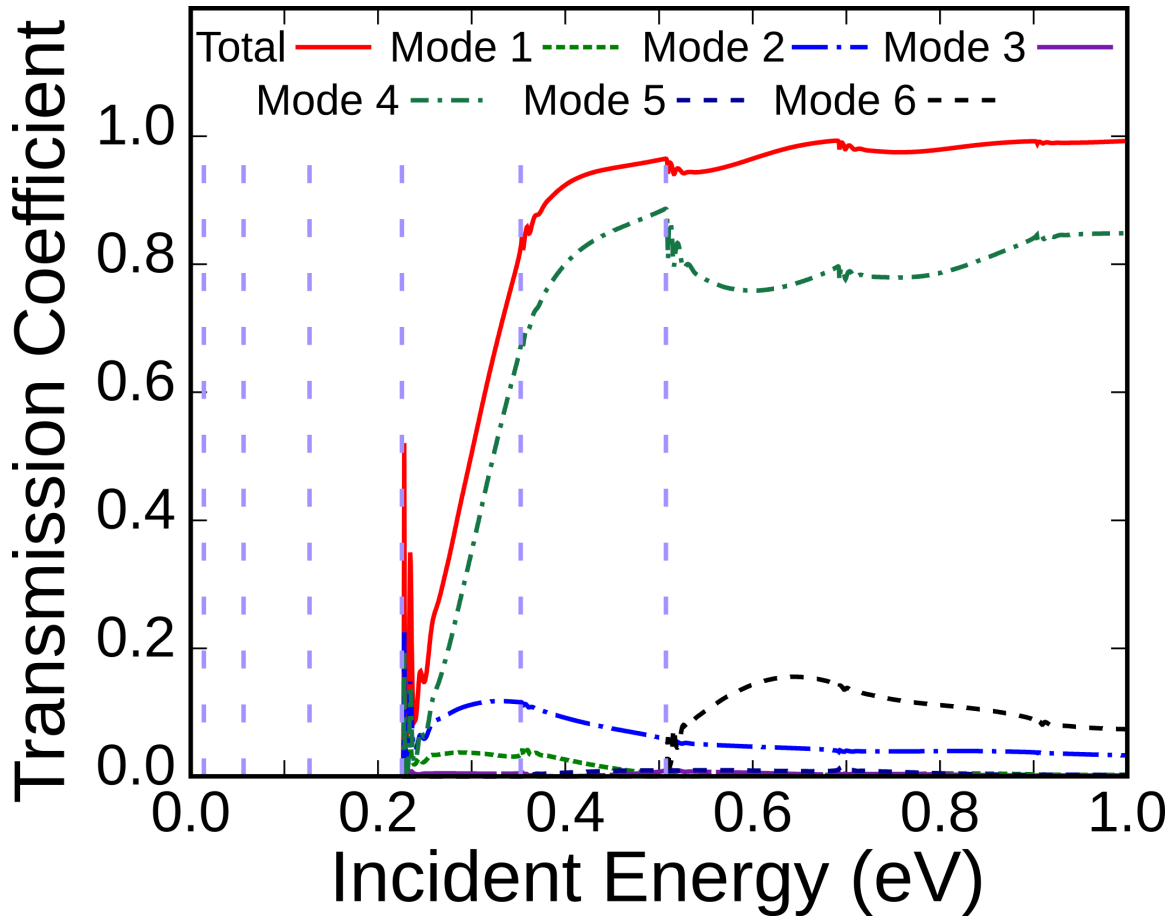


FIG. 51. The incident transmission versus energy plot for the lens scatterer, rotated 45 degrees, with an incident plane wave in mode $n=4$ is shown. Here we can see contribution from only even modes due to the symmetry of the incident mode being preserved by the bilaterally symmetric square scatterer in the waveguide. The thresholds for each transmitted mode correspond to new a channel being opened. These thresholds are indicated by the vertical dashed lines.

IV. CONCLUDING REMARKS

The usual picture of scattering as presented in books on quantum mechanics is to envision simple prepared states at $r \rightarrow -\infty$ that get scattered by a scattering center, and then those scattered waves are detected at $r \rightarrow \infty$. The ratio of the probability current density in the asymptotic region per unit incident flux of particles is defined as a measure of the scattering process. In nanoscale systems this concept requires major alterations since the asymptotic region is no longer obtained in actual structures. The complexity generated by the boundaries of the physical region in such systems being close to the active scattering region requires the new approach presented here. Only one textbook has explicitly shown the connection between variational methods, the action, and scattering theory.¹⁰ The fact that the scattering boundary conditions can be incorporated into the action integral provides us with a powerful and universal variational approach to scattering. When this method is implemented in the finite element framework, we are able to convert the Cauchy BCs into Dirichlet BCs through the use of stealth elements. In summary, we have that

- (i) Quantum scattering can be cast in an action integral framework with Cauchy BCs.
- (ii) The use of stealth or absorbing regions transforms the Cauchy BCs to Dirichlet BCs at the periphery with a substantial reduction in the computational complexity of the scattering problem at hand. The stealth parameter, α , is increased in a smooth manner (a cubic polynomial is used), so that no reflected wave is generated back into the waveguide.
- (iii) By introducing a source term we can have any wavefunction incident on the scattering region.
- (iv) The scattered wave, in both 1D and 2D scattering, is isolated so that partial wave analysis (Fourier decomposition into modes) can be performed *a posteriori*.
- (v) The use of interpolating polynomials with derivative continuity yields solutions with very high accuracy. The test calculations reported here yield transmission coefficients, wavefunctions, and evanescent modes with exquisite detail. Being a variational calculation, the level of accuracy can be improved systematically.

(vi) With the analysis being based on the action integral and its discretization into finite elements, we are able to consider scatterers of complex geometry, bent waveguides, and the open domain. This calculation results in a solution which goes beyond the First Born Approximation.

It is clear from the above that one has improved beyond the traditional First Born approximation and are able to treat multiple scatterers in a natural manner. We thus have at hand an excellent means of expanding scattering theory to its fullest details, and we hope to pursue this program of work even further.

-
- ¹ G. Gamow, Z. Phys. **51**, 204 (1928); Nature **122**, 805 (1928); Z. Phys. **52**, 510 (1928); *ibid.* **53**, 601 (1929).
- ² R W Gurney and E U Condon, Nature **122**, 439 (1928); Phys. Rev **33**, 127 (1929).
- ³ D. Bohm, *Quantum Theory* (Dover, NY, 1989).
- ⁴ R. Shankar, *Principles of Quantum Mechanics*, 2nd Ed. (Springer, NY, 1994).
- ⁵ C. Cohen-Tannoudji, B. Diu and F. Laloë, *Quantum Mechanics* Vol. 2 (Wiley Inter-Science, NY, 1977); translated from the French by S. R. Hemley, N. Ostrowsky and D. Ostrowsky.
- ⁶ J. R. Taylor, *Scattering Theory: The Quantum Theory of Nonrelativistic Collisions* (Dover, NY, 2006).
- ⁷ S. K. Adhikari, *Variational Principles and the Numerical Solution of Scattering Problems* (Wiley Inter-Science, NY, 1998).
- ⁸ M. L. Goldberger and K. M. Watson, *Collision Theory* (J. Wiley and Sons, NY, 1964).
- ⁹ R. G. Newton, *Scattering Theory of Waves and Particles*, 2nd Ed. (Springer-Verlag, NY, 1982).
- ¹⁰ L. R. Ram-Mohan, *Finite Element and Boundary Element Applications in Quantum Mechanics* (Oxford U.P., Oxford, UK, 2002).
- ¹¹ R. Courant and D. Hilbert, *Methods of Mathematical Physics* (Interscience Publishers, NY, 1953). Vol. 1, pp208–211.
- ¹² J. Goldstone and R. L. Jaffe, Phys. Rev. B **45**, 14100 (1991).
- ¹³ Philip F. Bagwell, Phys. Rev. B **41**, 10354 (1990).
- ¹⁴ Erkan Tekman and Philip F. Bagwell, Phys. Rev. B **48**, 2553 (1993).

- ¹⁵ M. Göppl, A. Fragner, R. Bianchetti, S. Filipp, J. M. Fink, P. J. Leek, G. Puebla, L. Steffen and A. Wallraff, *Journal of Appl. Phys.* **104**, 113904 (2008).
- ¹⁶ K. Lin and R. L. Jaffe, *Phys. Rev. B* **54**, 5750 (1996).
- ¹⁷ O. Olendski and L. Mikhailovska, *Phys. Rev. B* **67**, 035310 (2003).
- ¹⁸ Jens U. Nöckel and A. Douglas Stone, *Phys. Rev. B* **50**, 17415 (1994).